







Hydrodynamic instabilities of active jets

Marco Vona ¹, Isabelle Eisenmann ², Nicolas Desprat ², Raphaël Jeanneret ^{2,*},
Takuji Ishikawa ³ and Eric Lauga ^{1,†}

¹*Department of Applied Mathematics and Theoretical Physics, [University of Cambridge](#), Wilberforce Road, Cambridge CB3 0WA, United Kingdom*

²*Laboratoire de Physique de l'École normale supérieure, [ENS](#), [Université PSL](#), CNRS, Sorbonne Université, Université Paris Cité, F-75005 Paris, France*

³*Department of Biomedical Engineering, [Tohoku University](#), 6-6-01, Aoba, Aramaki, Aoba-ku, Sendai 980-8579, Japan*



(Received 28 March 2025; accepted 9 September 2025; published 6 November 2025)

Using a combination of theory, experiments, and numerical simulations, we investigate the stability of coherent structures in a suspension of strongly aligned active swimmers. We show that a dilute jet of pullers undergoes a pearling instability, while a jet of pushers exhibits a helical (or, in two dimensions, zigzag) instability. We further characterize the nonlinear evolution of these instabilities, deriving exact and approximate solutions for the spreading and mutual attraction of puller clusters, as well as the wavelength coarsening of the helical instability. Our theoretical predictions closely match the experimentally observed wavelengths, timescales, and flow fields in suspensions of photophobic algae, as well as results from direct numerical simulations. These findings reveal the intrinsic instability mechanisms of aligned active suspensions and demonstrate that coherent structures can be destabilized by the flows they generate.

DOI: [10.1103/pbzf-svnr](https://doi.org/10.1103/pbzf-svnr)

I. INTRODUCTION

Suspensions of active particles exhibit rich and diverse behaviors [1,2], such as accumulation near boundaries [3], flocking [4], enhanced aggregation and cluster formation [5], and phase-transitioning between solidlike and gaslike states [6]. Active swimmers have even been proposed as a vessel for the direct transport of cargo on the microscale, with applications to drug delivery and nanoscale assembly [7]. Due to long-range hydrodynamic interactions, actively driven flows often present much larger length scales than those characterizing the individual active particles [8–10], leading to collective motion and well-studied phenomena such as bacterial turbulence [11], enhanced tracer diffusivity [12], and long-range density modulations in the presence of inclusions [13].

Much is known about collective dynamics induced by biased motility in the presence of an external stimulus, such as light [14], magnetic fields [15], hydrodynamic shear [16], or gravity [17–20]. Much attention has in particular been given to the formation of macroscopic, beamlike concentrated structures with large particle density in active suspensions [17,19]. A classical mechanism leading to the formation of such structures is sedimentation [17,21–24], which, in combination with the particles' geometry, can result in self-enriching downwelling regions of high shear [25]. Numerical experiments have further revealed that the sole tendency of particles to align in response to external

*Contact author: raphael.jeanneret@phys.ens.fr

†Contact author: e.lauga@damtp.cam.ac.uk

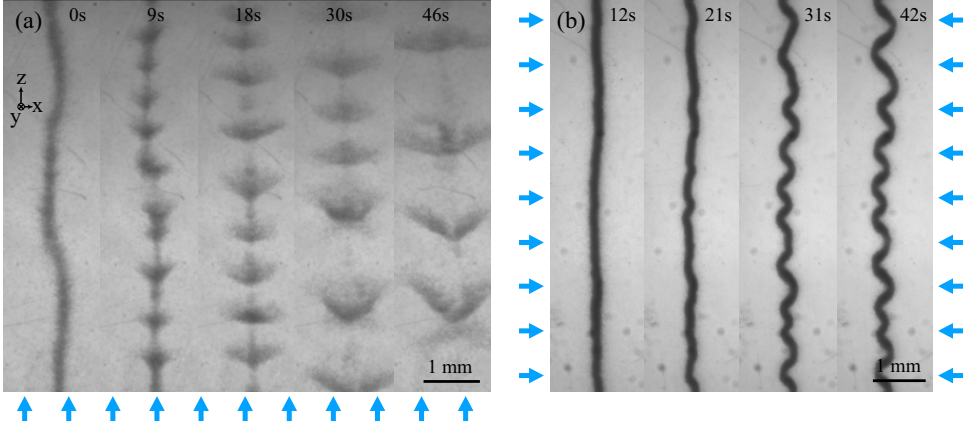


FIG. 1. Empirical observations motivating the theory developed in the paper. (a) Experiments with jets of negatively phototactic *C. reinhardtii* show that, upon setting the jet into motion by means of an axial light source (light direction $+\mathbf{e}_z$), the shape of the jet becomes unstable, breaking up into clusters. Over time, these spread out perpendicularly to the axis of the jet, before undergoing a “V”-shaped instability (top view). (b) Conversely, if the algae are rotated perpendicularly to the jet axis by means of side illumination, then the jet buckles (top view). Adapted from Ref. [37].

stimuli, such as light [14], magnetic fields [15], oxygen concentration [26,27], or the direction of gravity [19,28,29], may be sufficient for the formation of coherent slender structures, even in the absence of sedimentation. In the paper, we will refer to these structures as *active jets*.

To our knowledge, a controlled experimental realization of such active jets is still lacking. The main difficulty is that cells must be consistently well aligned to prevent the jet from flying apart. This is only possible if cells are made to reorient on a timescale which is much faster than that of the flow itself. For experiments involving gravitaxis or gyrotaxis, typical reorientation timescales for the model organism *Chlamydomonas reinhardtii* are known to be on the order of seconds [18], which is comparable to the observed flow timescales. In this situation, the jet would therefore quickly become incoherent.

As a result of these experimental challenges, studies of active jets have been mostly computational in nature [27,30]. An intriguing feature of such jets is that they are fundamentally unstable, exhibiting instabilities driven by cell activity. Notably, numerical studies [30] of concentrated gyrotactic plumes of strongly active sedimenting squirmers [31] demonstrated actively driven shape instabilities that depended on whether the swimmers were “pushers” [32] or “pullers” [33]. Specifically, pusher jets were prone to a helical instability [30], while puller jets presented a pearling instability [34]. A similar numerical treatment recovered a pearling instability for phototactic pullers under confinement [27]. The origin of these instabilities can be rationalized theoretically by means of simplified one-dimensional (1D) setups [35,36], with the underlying physical mechanism related to the active stresses exerted by the swimmers.

In the joint article [37], we propose a novel experimental way to create stable active jets by steering phototactic cells via strong illumination. Negatively phototactic *C. reinhardtii* were loaded into a chamber, which was placed between two parallel arrays of LED lights. After a few minutes, the light-fleeing cells formed a dense band at the center of the chamber. If the side LEDs were switched off and a collimated LED light parallel to the band was switched on, then the jet was set into motion and quickly broke up into clusters [time-lapse images shown in Fig. 1(a)], consistently with predictions for the first instability (pearling) from simulations [30]. In order to reproduce the zigzag instability for pusher cells [30], we next exploited the fact that increasing the intensity of the lateral LEDs strengthened the alignment of algae perpendicularly to the band’s axis, producing microscopic dipolar flows similar to those of pushers aligned with the jet axis.

Remarkably, this setup was then able to reproduce the pusher zigzag instability [the experimental results are summarized in Fig. 1(b)].

In the current article, we provide a fully three-dimensional dilute continuum model explaining the numerically [2,30] and experimentally [37] observed instabilities of an active jet of aligned cells. Extending previous one-dimensional studies [35,36] to finite-sized jets of active particles, we compute the linearized time evolution of a perturbation of the jet geometry. We recover the aforementioned pearling and helical/zigzag instabilities for both cylindrical jets and two-dimensional “sheets” of swimmers and determine the corresponding wavelengths and growth rates. We then extend our theoretical framework to investigate the long-term jet dynamics. We numerically and analytically determine the time evolution of the clusters resulting from the breakup of a puller jet, deriving both exact solutions in special cases as well as long-term similarity solutions. We furthermore obtain approximate evolution equations for the nonlinear dynamics of a buckled pusher jet, determining the driving flows by means of asymptotic methods. We further compare our findings with experiments [37], demonstrating quantitative agreement between the wavelength, growth rate and flow fields. To corroborate the theory, we finally perform agent-based numerical simulations implementing the Stokesian dynamics method and validate our prediction for the wavelength and growth rate of each instability type, as well as the long-term dynamics.

The paper is structured as follows: In Sec. II, we introduce the different jet geometries considered and derive the continuum model for the suspension, consisting of effective equations for the flow and the swimmer volume fraction. We then specialize these equations to the limiting case of a jet with a sharp interface and a constant swimmer volume fraction (Sec. IID). We hence carry out a linear stability analysis in the three-dimensional case (Sec. III) and in the two-dimensional setup (Sec. IV). We next consider the long-term evolution of the puller jet (Sec. V), and the evolution of a buckled pusher jet (Sec. VI). We finally compare our analytical results to numerical simulations and experiments (Secs. VII A and VII B, respectively).

II. CONTINUUM MODELLING OF ACTIVE JETS

Our first goal is to establish the continuum model we will work within, and to specialize it to the case of active jets in order to derive effective evolution equations for their shape. Our analysis relies on the assumptions of zero diffusion for the swimmers (both in position and orientation), and of constant swimming direction (which will be physically justified by considering the various timescales involved). The effect of the swimmers on the flow is coarse-grained into an effective active stress [8,9,38] capturing the average bulk stresses exerted by the particles on the fluid [18,39,40]. As we will see, under these assumptions, the time evolution of a swimmer-laden region is driven by the Stokes equations, paired with suitable continuity and force-balance boundary conditions.

A. Jet geometry

Throughout this paper, we consider the case of a dilute suspension of neutrally buoyant (and hence force free), identical spherical swimmers in an unbounded fluid. The swimmers align in response to an external stimulus, such as light, gravity, magnetic fields, or chemical gradients. We denote the orientation of each swimmer by a unit vector \mathbf{p} and take the preferred direction for alignment to be \mathbf{e}_z . We let the swimmer radius be a_s (and the swimmer volume be V), and we denote by U_s the (constant) swimming speed of an isolated swimmer. Finally, we use $\phi(\mathbf{x}, t)$ to indicate the swimmer volume fraction, with $\phi \ll 1$ in the dilute limit. We assume that all swimmers can initially be found inside a specified region of space, which corresponds to the base state of the jet.

Two different geometries will be considered (Fig. 2), motivated by experiments:

- (1) Cylindrical jets: All swimmers are initially positioned in the domain given by $0 \leq r \leq a$, $-\infty < z < \infty$ in cylindrical coordinates. This is the case illustrated in Fig. 2(a).
- (2) Two-dimensional jets: All swimmers are initially positioned in a sheet of finite thickness, given by $-a \leq x \leq a$, $-\infty < y, z < \infty$ in Cartesian coordinates. The sheet is taken to be

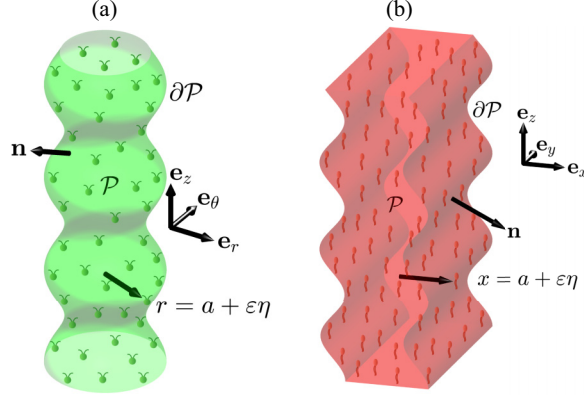


FIG. 2. Schematic illustration of the two jet geometries considered in our modeling. (a) Cylindrical active jet of radius a . (b) Two-dimensional active jet of half-width a . The fluid outside the jet is a simple Newtonian solvent with no active particles. In each case, we analyze the growth of a boundary perturbation of magnitude $\varepsilon\eta \ll a$. Our analysis concerns both pushers and pullers for each geometry (the above sketch only illustrates particular examples).

homogeneous in the y direction, so that the dynamics is effectively restricted to the xz plane. This case is sketched in Fig. 2(b).

B. Modelling assumptions

As mentioned above, in order for our model to accurately describe the experimental jet, which maintains a sharp boundary at all times, two further assumptions are needed:

(1) Swimmers are clamped so that their swimming direction is constantly along the axis of the unperturbed jet. In other words, $\mathbf{p} \equiv \mathbf{e}_z$ at all times.

(2) Spatial diffusion is negligible, so that swimmers do not leave the jet as a result of stochastic effects.

If swimmers were not aligned (assumption 1), then variations in swimming directions due to the flow or rotational diffusion would cause the jet to fly apart over time. Similarly, translational diffusion (assumption 2) would smear out the boundary of the jet, which is at odds with experiments. Physically, assuming that $\mathbf{p} \equiv \mathbf{e}_z$ at all times is appropriate whenever the reorientation timescale B is much shorter than the flow timescale T (corresponding to the onset of the instability). Indeed, in the dilute limit, the evolution of the swimming direction can be described by the Faxén equation [1,19,40]

$$\dot{\mathbf{p}} = \frac{1}{2B}(\mathbf{I} - \mathbf{p}\mathbf{p}) \cdot \mathbf{e}_z + \frac{1}{2}\boldsymbol{\omega}(\mathbf{x}, t) \times \mathbf{p}, \quad (1)$$

where $\boldsymbol{\omega} = \nabla \times \mathbf{u}$ is the flow's vorticity. The clamped approximation ($\mathbf{p} \equiv \mathbf{e}_z$) is valid whenever $\|\boldsymbol{\omega}\| \ll B^{-1}$ or, in other words, when $B \ll L/U$. The right-hand side coincides with the advective timescale, which, as we will later see, coincides with the flow timescale T . Assumptions 1 and 2 are sufficient to formulate a theoretical framework for the study of active jets. The applicability of these assumptions to our specific experimental setup will be discussed in Sec. VII B.

C. Equations of motion

Having specified the geometry, we now turn our attention to the derivation of the flow equations.

1. The active stresslet

On the scale of an individual swimmer, the activity and stimulus-driven taxis are associated with a stresslet S_{ij} and, in the cases, e.g., of magnetotaxis and gravitaxis (but not for phototaxis or chemotaxis), a torque L_i on the fluid. Indeed, while for magnetotaxis and gravitaxis swimmers are subject to a physical, orientation-dependent torque (provided by the magnetic field or gravity, respectively), in the case of phototaxis or chemotaxis, reorientations are achieved purely by swimming, which is inherently torque free.

It is a classical result that the stresslet and torque of a given swimmer are explicitly given by [40]

$$S_{ij} = \int_{\partial B} \left[\frac{1}{2} (\sigma_{ik} x_j + \sigma_{jk} x_i) b_k - \mu (v_i b_j + v_j b_i) - \frac{1}{3} (x_k \sigma_{kl} b_l) \delta_{ij} \right] dA, \quad (2)$$

$$L_i = \varepsilon_{ijk} \int_{\partial B} \sigma_{jl} x_k b_l dA, \quad (3)$$

where ∂B is the closed surface of the swimmer, μ is the dynamic viscosity of the fluid, v_i is the variation in the background flow due to the swimmer, σ_{ij} is the variation in the background hydrodynamic stress due to the swimmer, b_i is the local unit normal to the swimmer's body, and ε_{ijk} is the antisymmetric Levi-Civita tensor.

The leading-order values of S_{ij} and L_i are the same as for an isolated swimmer, up to corrections (caused by particle-particle interactions) proportional to the swimmer volume fraction, which can be neglected in the dilute limit. In particular, if the swimming direction is clamped, then the torque is purely a response to particle-particle interaction, so $L_i = \mathcal{O}(\phi)$. We can therefore assume $L_i = 0$ at leading order in ϕ , regardless of whether organisms are torque free or not. In this sense, while our experiments focus on the special case of phototaxis, our dilute modeling approach provides a unifying description of a multitude of taxes under different physical mechanisms.

A further simplification may be inferred by noting that, while S_{ij} is *a priori* a traceless symmetric tensor with five independent components, in the case of steady axisymmetric swimmers the number of independent components reduces to just one. This allows us to write [40]

$$S_{ij} = S(p_i p_j - \frac{1}{3} \delta_{ij}), \quad (4)$$

where S is a scalar parameter intrinsic to the swimmer: “puller” swimmers have $S > 0$, while “pushers” have $S < 0$ [8,9].

2. Collective flow equations

The superposition of all the dipolar flows created by the swimmers results in a macroscopic, continuum flow with velocity $\mathbf{u}(\mathbf{x}, t)$. A classical calculation by Batchelor [39] shows that one may define an effective stress for this flow, given by a divergence-free stress tensor obtained by suitable averaging over the fluid-particle system within the jet. When the swimming direction is clamped, the result is

$$\Sigma_{ij}^- = -q^- \delta_{ij} + \mu \left(\frac{\partial u_i^-}{\partial x_j} + \frac{\partial u_j^-}{\partial x_i} \right) + \frac{S\phi}{V} p_i p_j, \quad (5)$$

where q denotes the pressure and a “ $-$ ” superscript denotes the interior of the jet. Outside the jet, the particle concentration is 0 and the stress tensor reduces to the Newtonian value

$$\Sigma_{ij}^+ = -q^+ \delta_{ij} + \mu \left(\frac{\partial u_i^+}{\partial x_j} + \frac{\partial u_j^+}{\partial x_i} \right), \quad (6)$$

where a “ $+$ ” superscript denotes the exterior of the jet.

We note that, in order to be able to identify Eq. (4) with the particle stress, we implicitly assumed the suspension to be locally statistically homogeneous [39]. In other words, the properties of the suspension should vary on a length scale much larger than the swimmer size. While this assumption

is apparently violated at the sharp boundary of the jet, in Appendix A 1 we explicitly show that one may think of the discontinuity as the leading-order approximation of a smooth concentration field, for which the continuum assumption is valid.

Effective equations for the interior and exterior of the jet may now be derived by requiring stresses to balance on every material element [Eqs. (7a), (8a), and (9a)]. In addition, we impose incompressibility conditions on the velocity fields [Eqs. (7b) and (8b)], as well as continuity of velocity at the jet boundary [Eq. (9b)] in order to avoid infinite stresses:

Jet		Exterior		Boundary	
$\partial_j \Sigma_{ij}^- = 0$	(7a)	$\partial_j \Sigma_{ij}^+ = 0$	(8a)	$\Sigma_{ij}^- n_j = \Sigma_{ij}^+ n_j$	(9a)
$\partial_i u_i^- = 0$	(7b)	$\partial_i u_i^+ = 0$	(8b)	$u_i^- = u_i^+$	(9b)

where \mathbf{n} denotes the local unit normal to the jet boundary (Fig. 2). In Appendix A 1, we show that Eqs. (7a) through (9b) may be derived via the method of matched asymptotics as the leading-order flow equations for a smooth but rapidly varying concentration profile. Alternatively, Eqs. (7a) through (9b) may be postulated empirically by writing the bulk flow as the superposition of the swimmers' dipolar flows [10], without appealing to statistical homogeneity or stress-balance arguments; such an alternative derivation is presented in Appendix A 2.

3. Swimmer conservation

Finally, in order to close the system, we need an evolution equation for the swimmer concentration ϕ . Individual swimmer motion is a combination of self-propulsion along the constant swimming direction, and advection by the flow. Therefore, if $\mathbf{x}(t)$ denotes the position of a swimmer, then

$$\dot{\mathbf{x}}(t) = \mathbf{u}(\mathbf{x}, t) + U_s \mathbf{e}_z. \quad (10)$$

The corresponding evolution of the volume fraction is found by imposing swimmer conservation, i.e., $d(\phi \mathcal{W})/dt = 0$, where \mathcal{W} is a small volume. Because the right-hand side of Eq. (10) is divergence free, $d\mathcal{W}/dt = 0$ and the volume fraction is constant along swimming trajectories, i.e.,

$$\frac{d}{dt} \phi[\mathbf{x}(t), t] = 0. \quad (11)$$

Note that the result in Eq. (11) is equivalent to the standard Smoluchowski equation [8,9] for a smooth field ϕ , given by $\phi_t + \nabla \cdot [(\mathbf{u} + U_s \mathbf{e}_z)\phi] = 0$, which is the same as $d\phi/dt = 0$.

D. Constant-concentration solution

We now restrict our attention to a special class of solutions of Eqs. (7a)–(9b), (11). We denote the region of space occupied by the jet at time t by $\mathcal{P}(t)$. As a model for our experiments [37], we restrict our attention to the case in which, initially, the swimmer concentration is uniform inside the jet. Mathematically, at time $t = 0$, the swimmer volume fraction is therefore taken to be

$$\phi(\mathbf{x}, t = 0) = \begin{cases} \phi_0 & \mathbf{x} \in \mathcal{P}(0), \\ 0 & \mathbf{x} \notin \mathcal{P}(0), \end{cases} \quad (12)$$

for some constant ϕ_0 . The swimmer conservation Eq. (11) then admits the solution

$$\phi(\mathbf{x}, t) = \begin{cases} \phi_0 & \mathbf{x} \in \mathcal{P}(t), \\ 0 & \mathbf{x} \notin \mathcal{P}(t), \end{cases} \quad (13)$$

where $\mathcal{P}(t)$ is the advected image of $\mathcal{P}(0)$ under Eq. (10). The fact that the concentration is constant inside the jet offers considerable simplifications to our model. Indeed, the bulk stress-balance equation (7a) in the jet [with stress tensor in Eq. (5)] reduces to the Stokes equation $\partial_i q^- = \mu \partial_j \partial_j u_i^-$, and the active component of the stress only appears in boundary condition (9a). Referring to Fig. 2 for the notation, the simplified equations that we work with are therefore

$\mathbf{x} \in \mathcal{P}(t)$	$\mathbf{x} \notin \mathcal{P}(t)$	$\mathbf{x} \in \partial \mathcal{P}(t)$
$\partial_i q^- - \mu \partial_j \partial_j u_i^- = 0$ (14a)	$\partial_i q^+ - \mu \partial_j \partial_j u_i^+ = 0$ (15a)	$\Sigma_{ij}^- n_j = \Sigma_{ij}^+ n_j$ (16a)
$\partial_i u_i^- = 0$ (14b)	$\partial_i u_i^+ = 0$ (15b)	$u_i^- = u_i^+$ (16b)
		$\dot{x}_i = u_i + U_s p_i$ (16c)

Physically, the active stress only appears at the boundary [Eq. (16a)] because the bulk dipoles cancel each other in a uniform concentration field. Consequently, only the boundary forces remain unbalanced, leading to fluid flow. This intuition is made precise in Appendix A 2.

III. LINEAR STABILITY OF A CYLINDRICAL ACTIVE JET

We now specialize the above framework to a particular jet geometry, specifically to the case where $\mathcal{P}(0)$ is the cylinder $0 \leq r \leq a$, $-\infty < z < \infty$ [Fig. 2(a)]. The applicability of this idealized geometry to our specific experimental setup is discussed in Sec. VII B. As a reminder, the swimmer volume fraction inside the jet is constant ($\phi \equiv \phi_0$), and the swimming direction is vertically clamped ($\mathbf{p} \equiv \mathbf{e}_z$). Our goal is to study the evolution of the shape of the jet, as given by Eqs. (14a)–(16c), when the location of the jet boundary is perturbed. In particular, we are interested in whether a given boundary perturbation grows or decays with time. We define a boundary perturbation as “stable” if it decays to zero over time, and “unstable” if it grows. The term “stability” will therefore always refer to the shape of the jet.

A. Base state

The base state corresponds to an everywhere-vanishing velocity field, i.e.,

$$\mathbf{u}_0^\pm = \mathbf{0}, \quad q_0^\pm = 0, \quad \Sigma_0^+ = \mathbf{0}, \quad \Sigma_0^- = \frac{S\phi_0}{V} \mathbf{e}_z \mathbf{e}_z, \quad (17)$$

which is easily verified to be a solution of Eqs. (14a)–(16c). In particular, the stress boundary condition (16a) is satisfied, as the orientation of the force dipoles exerted by the swimmers is purely axial, with no component perpendicular to the jet boundary. The kinematic boundary condition (16c) is likewise satisfied, as points at the boundary are advected according to $\dot{\mathbf{x}} = U_s \mathbf{e}_z$, which leaves the shape of the jet unchanged. Notably, if \mathbf{p} was not fixed and, instead, diffused rotationally, then boundary swimmers would migrate outwards, and (17) would not be a steady solution of Eqs. (14a)–(16c).

B. $\mathcal{O}(\varepsilon)$ Flow: Linear perturbation

We now introduce a small boundary perturbation of order ε , which leaves the active stresses unbalanced at the boundary, resulting in a net ambient flow and motion of the jet. More precisely, we let the time-dependent deformed jet boundary be given by $r = R(z, \theta, t)$, with cylindrical coordinates $-\infty \leq z \leq \infty$ and $0 \leq \theta < 2\pi$ [Fig. 2(a)]. In the limit of a small distortion ($|\varepsilon| \ll 1$), we may classically exploit linearity to assume that the perturbation consists of a single Fourier

mode, i.e.,

$$R = a + \varepsilon \eta(z, \theta, t) = a(1 + \varepsilon e^{st+ikz+in\theta}). \quad (18)$$

We may assume $k \geq 0$, $n \in \mathbb{Z}_{\geq 0}$, as different sign combinations are equivalent to simply reflecting the setup. We now aim to solve equations Eqs. (14a)–(16c) to determine the growth rate $\text{Re}(s)$ as a function of the axial and angular wave numbers, k and n . As is standard, we may then deduce which perturbations grow and which decay by noting that stable Fourier modes have $\text{Re}(s) < 0$, while unstable modes have $\text{Re}(s) > 0$.

In order to solve for s , we expand the velocities, pressures, and stresses in the small parameter ε as

$$\mathbf{u}^\pm = \mathbf{u}_0^\pm + \varepsilon \mathbf{u}_1^\pm + \mathcal{O}(\varepsilon^2), \quad (19a)$$

$$q^\pm = q_0^\pm + \varepsilon q_1^\pm + \mathcal{O}(\varepsilon^2), \quad (19b)$$

$$\boldsymbol{\Sigma}^\pm = \boldsymbol{\Sigma}_0^\pm + \varepsilon \boldsymbol{\Sigma}_1^\pm + \mathcal{O}(\varepsilon^2), \quad (19c)$$

where the base state corresponds to Eq. (17). To study the evolution of the boundary disturbance $\varepsilon \eta$, we must expand the bulk flow equations and boundary conditions (14a)–(16c) up to and including $\mathcal{O}(\varepsilon)$. Following notation shown in Fig. 2(a), at order $\mathcal{O}(\varepsilon)$,

$0 \leq r \leq a$	$a < r < \infty$	$r = a$
$\mu \nabla^2 \mathbf{u}_1^- = \nabla q_1^- \quad (20a)$	$\mu \nabla^2 \mathbf{u}_1^+ = \nabla q_1^+ \quad (21a)$	$(\boldsymbol{\Sigma}_1^+ - \boldsymbol{\Sigma}_1^-) \cdot \mathbf{e}_r = -\frac{S\phi_0}{V} \eta_z \mathbf{e}_z \quad (22a)$
$\nabla \cdot \mathbf{u}_1^- = 0 \quad (20b)$	$\nabla \cdot \mathbf{u}_1^+ = 0 \quad (21b)$	$\mathbf{u}_1^+ = \mathbf{u}_1^- \quad (22b)$
	$\lim_{r \rightarrow \infty} \mathbf{u}_1^+ = \mathbf{0} \quad (21c)$	$\frac{\partial \eta}{\partial t} + U_s \frac{\partial \eta}{\partial z} = \mathbf{u}_1^\pm \cdot \mathbf{e}_r. \quad (22c)$

Physically, Eq. (22a) shows that the flow is driven by the boundary stresslets, while Eq. (22c) reflects the fact that, for a clamped swimming direction, the swimming speed only causes the jet to rigidly translate along \mathbf{e}_z .

We may integrate Eqs. (20a)–(22c) exactly, thus determining the velocity and pressure fields \mathbf{u}_1^\pm , q_1^\pm up to a multiplicative constant; Eq. (22c) then provides a condition for the existence of nonzero solutions to Eqs. (20a) through (22b), which uniquely determines the growth rate. The details of the calculation are provided in Appendix B, and here we only present the final result for the growth rate $\text{Re}(s)$, which is

$$\text{Re}(s) = \frac{S\phi_0}{2\mu V} \frac{I_n(\xi)[K_n(\xi)(2n^2 + \xi^2) - n\xi K_{n+1}(\xi)] - I_{n+1}(\xi)[\xi^2 K_{n+1}(\xi) - n\xi K_n(\xi)]}{\xi I_n(\xi)K_{n+1}(\xi) + \xi K_n(\xi)I_{n+1}(\xi)}, \quad (23)$$

where $\xi = ak$ is the dimensionless axial wave number, while the I_n and K_n are modified Bessel functions [41,42]. Our analysis also reveals that $\text{Im}(s) = -ikU_s$. Therefore, as suggested by Eq. (22c), the swimming speed only leads to net upward motion of the jet without affecting the extend of the boundary distortion and therefore the stability characteristics.

C. Analysis of the growth rate

As expected, Eq. (23) shows that the timescale of the instability is set by the stresslet strength S . The dependence of the growth rate $\text{Re}(s)$ on the wave numbers ξ and n is shown in Fig. 3. We may thus fully determine the modes (ξ, n) that cause the perturbation to grow or decay for pushers

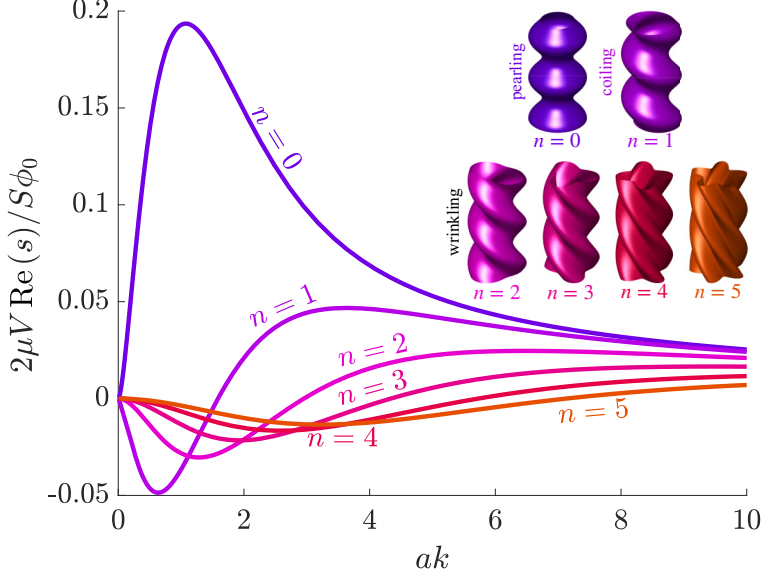


FIG. 3. Plot of dimensionless growth rate $2\mu V \text{Re}(s)/S\phi_0$ as a function of the dimensionless wave number for $0 \leq n \leq 5$. Inset shows the corresponding shapes of the jet boundary. The $n = 0$ mode corresponds to axisymmetric pearling, $n = 1$ corresponds to helical buckling (with circular cross section), while $n \geq 2$ are higher-order wrinkling modes with centerline parallel to \mathbf{e}_z . Note that if $S < 0$ (pushers), then the graph of $\text{Re}(s)$ as a function of ak has the opposite sign to the curves plotted above, so the stable/unstable regions are flipped.

($S < 0$) and pullers ($S > 0$). We next provide a summary of the results, with further details of the asymptotic calculations given in Appendix C. The two main stability results are as follows:

(1) Jets of pullers (i.e., with $S > 0$) are unstable to all axisymmetric modes $(\xi, 0)$, and to nonaxisymmetric modes (ξ, n) with $n \geq 1$ for small axial wavelengths ($\xi \gtrsim 2^{1/2}n$).

(2) Jets of pushers ($S < 0$) are only unstable to nonaxisymmetric modes (ξ, n) with $n \geq 1$ and large axial wavelengths ($\xi \lesssim 2^{1/2}n$).

In other words, puller jets are unstable whenever the axial wavelength is much smaller than the angular wavelength, while the situation is reversed for pushers. This may be rationalized by noting that the puller dipole flow tends to relax angular distortions, since pullers eject fluids sideways. On the other hand, pushers drive the opposite flow to pullers, thereby enhancing wrinkly modes. Therefore, if most of the distortion is in the θ direction (i.e., $\xi \ll n$), then pullers have a stabilizing effect, and pushers have a destabilizing effect. The opposite occurs if most of the distortion is axial (i.e., $\xi \gg n$). In particular, since angular variations are much slower than axial ones (and hence negligible) for $\xi \rightarrow \infty$, the resulting jet is unstable for pullers and stable for pushers, with

$$\text{Re}(s) \sim \frac{S\phi_0}{8\mu V\xi}, \quad \xi \rightarrow \infty \quad (24)$$

regardless of n .

D. Fastest-growing modes

A second, more experimentally relevant question, concerns the nature of the instability observed in a laboratory setting. In the context of linearized theory, any perturbation in the shape of a real-world jet may be decomposed into Fourier modes of the form (18), each growing or shrinking over time with growth rate given by Eq. (23). The observed mode in a given jet will therefore be the pair (ξ, n) which maximizes $\text{Re}(s)$. This allows us to predict the experimentally observed instability

types for pushers and pullers. Like before, we refer to Appendix C for the mathematical details. The main results are as follows:

(1) The fastest-growing mode for a jet of pullers ($S > 0$) is the axisymmetric one ($n = 0$) with wave number $\xi = \xi^* \sim 1.0750$. This corresponds to a pearling instability. The selected instability wavelength evaluates to $\lambda^* \sim 5.8447 \times a$, while the growth rate is $\text{Re}(s^*) \sim 0.0968 \times S\phi_0/\mu V$.

(2) The fastest-growing mode for a jet of pushers ($S < 0$) is the helical one ($n = 1$) with wave number $\xi = \xi^* \sim 0.6350$. The selected instability wavelength evaluates to $\lambda^* \sim 9.8943 \times a$, while the growth rate is $\text{Re}(s^*) \sim -0.0243 \times S\phi_0/\mu V$.

Interestingly, the wavelength is in each case only set by the initial jet radius a , and is independent of ϕ_0 (the only dimensionless quantity in the problem). This is because, in the dilute limit, the flow scales linearly with ϕ_0 , leaving wavelengths unaffected. The growth rate for the puller jet is also faster (by a factor of about 4) than the growth rate of a jet of pusher with the same value of $|S|$. Finally, for both swimmer types, higher-ordered wrinkling modes grow on progressively slower timescales. In Appendix C, we show in particular that the n th mode grows like $\text{Re}(s) \sim 0.02 \times S\phi_0/(\mu V n)$ for pullers and $\text{Re}(s) \sim 0.03 \times |S|\phi_0/(\mu V n)$ for pushers.

E. Oscillating stresslets

In the real biological system, the stresslet strength S for *C. reinhardtii* is not time independent. Rather, $S(t)$ oscillates around its mean value during the algae's beating pattern, switching from $S > 0$ during the power stroke to $S < 0$ during the recovery stroke [43]. Furthermore, due to the large beat frequency (50 Hz), the microscopic flows driven by the swimmers are unsteady beyond about 20 swimmer radii of each alga [43].

While accurately modeling such effects appears very challenging, we comment on the simplest case of spatially independent stresslet strength $S(t)$ and swimming speed $U_s(t)$, i.e., synchronous beating of all swimmers. Assuming the viscosity of the fluid to be sufficiently large as to overdamp any inertial effects, the stability of the active jet from Sec. III A and Sec. III B can be analyzed by replacing the term e^{st} in Eq. (18) with a generic function $e^{s(t)}$ (with $s(0) = 0$). Linear stability analysis then readily provides

$$\text{Re}(s) = \frac{\phi_0}{2\mu V} \frac{I_n(\xi)[K_n(\xi)(2n^2 + \xi^2) - n\xi K_{n+1}(\xi)] - I_{n+1}(\xi)[\xi^2 K_{n+1}(\xi) - n\xi K_n(\xi)]}{\xi I_n(\xi)K_{n+1}(\xi) + \xi K_n(\xi)I_{n+1}(\xi)} \int_0^t S(t') dt'. \quad (25)$$

For a rapidly oscillating stresslet with period-averaged value $\langle S(t) \rangle$, Eq. (25) is approximately equivalent to Eq. (23) with S replaced by $\langle S(t) \rangle$. In other words, our analysis remains approximately valid (at least in simple cases) for time-dependent swimming gaits, with an “effective” stresslet strength $\langle S(t) \rangle$. We expect a similar conclusion to hold when inertia is present, since rapidly oscillating swimmers should interact primarily via their period-averaged flows.

IV. LINEAR STABILITY OF A TWO-DIMENSIONAL ACTIVE SHEET

As a natural extension of the previously described cylindrical jet, in this section we consider the stability of an infinite sheet jet given by $-a \leq x \leq a$, $-\infty < y, z < \infty$ in Cartesian coordinates [setup shown in Fig. 2(b)]. We assume that the sheet stays homogeneous in the y direction, so that the dynamics is effectively confined to the xz plane. The relevance of this geometry to our experiments will be addressed in Sec. VII B.

As in Sec. III, we aim to understand if a given perturbation to the boundary of the sheet tends to grow or shrink with time, depending on whether the swimmers are pushers or pullers. Mathematically, we perturb the sheet boundary so that, for $t > 0$, the swimmers are located in $X^-(z, t) \leq x \leq X^+(z, t)$. We consider two forms of the perturbation (Fig. 4):

- (1) Sinuous (i.e., in phase): $X^+ = a(1 + \varepsilon e^{st+ikz})$, $X^- = a(-1 + \varepsilon e^{st+ikz})$;
- (2) Varicose (i.e., antiphase): $X^+ = a(1 + \varepsilon e^{st+ikz})$, $X^- = a(-1 - \varepsilon e^{st+ikz})$.

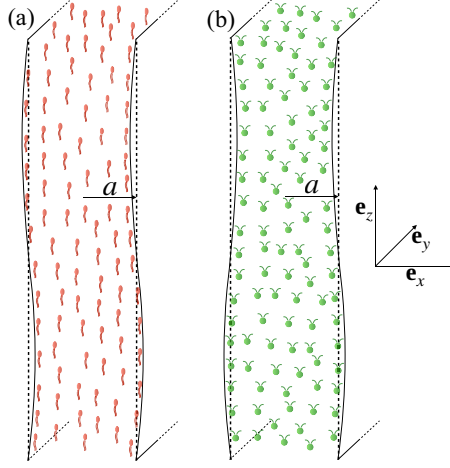


FIG. 4. Schematic representation of the sheet geometry and the two perturbations considered: (a) sinuous perturbation (i.e., in phase). (b) Varicose perturbation (i.e., antiphase).

In each case, we seek to determine the growth rate $\text{Re}(s)$, which dictates the stability of the perturbation depending on whether $\text{Re}(s) > 0$ (unstable) or $\text{Re}(s) < 0$ (stable). As before, we provide the details of the calculation in Appendix D and only state the main results:

- (1) In the case of a sinuous perturbation, the growth rate is given by

$$\text{Re}(s) = -\frac{S\phi_0}{2\mu V}\xi e^{-2\xi}, \quad (26)$$

where the dimensionless wave number is again $\xi := ak$. Therefore, a sinuous perturbation is always unstable for pushers, consistently with the three-dimensional case (as a sinuous perturbation is the two-dimensional equivalent of a helical mode in three dimensions). The most unstable wave number, which corresponds to the one measured in experiments, is $\xi = \xi^* = 1/2$. The selected instability wavelength is therefore $\lambda^* = 4\pi a \sim 12.5664 \times a$, while the growth rate is predicted to be $\text{Re}(s^*) \sim -0.0920 \times S\phi_0/\mu V$.

- (2) In the case of a varicose perturbation, the growth rate is given by

$$\text{Re}(s) = \frac{S\phi_0}{2\mu V}\xi e^{-2\xi}. \quad (27)$$

Therefore, a varicose perturbation is always unstable for pullers, consistently with the three-dimensional case (as a varicose perturbation is the two-dimensional equivalent of three-dimensional pearling). As in the previous case, the most unstable wave number is $\xi = \xi^* = 1/2$. The selected instability wavelength is therefore $\lambda^* = 4\pi a \sim 12.5664 \times a$, while the growth rate is given by $\text{Re}(s^*) \sim 0.0920 \times S\phi_0/\mu V$.

For both instabilities, $\text{Im}(s) = -ikU_s$, corresponding to net upwards translation of the jet, as was the case in Sec. III.

We conclude with the following important observation: Suppose that the particles had zero swimming speed and were oriented along the x axis instead of the z axis, so that $\mathbf{p} = -\text{sgn}(\mathbf{x})\mathbf{e}_x$ and $\mathbf{S} = S(\mathbf{e}_x\mathbf{e}_x - \mathbf{I}/3)$. In this case, the two instabilities would still be observed, but they would be reversed, i.e., a sheet of rotated pushers would now be prone to pearling and a sheet of rotated pullers would now buckle. This follows straightforwardly from the calculation in Appendix D, and it is primarily a consequence of the fact that a sheet of rotated stresslets exerts a boundary stress

$$S\mathbf{e}_x(\mathbf{e}_x \cdot \mathbf{n}) = S\mathbf{n} - S\mathbf{e}_z(\mathbf{e}_z \cdot \mathbf{n}). \quad (28)$$

Since the $S\mathbf{n}$ term merely corresponds to a constant pressure, the flow driven by the rotated stresslet is the same as the flow driven by axial stresslet of strength $-S$. This reflects the fact that, in two

dimensions, the flow field of a pusher and a puller stresslet of the same absolute magnitude are identical up to a 90° rotation. Therefore, a varicose instability is unstable for a sheet of rotated pushers (identical to axial pullers), and vice versa for a sinuous perturbation.

V. LONG-TERM NONLINEAR EVOLUTION OF PULLER CLUSTERS

After a puller jet breaks up into clusters, these are observed to flatten and stretch laterally under the effect of the internal active stresses [Fig. 1(a)]. This regime sets in once the initial varicose perturbation is well developed.

We now demonstrate that exact solutions for this long-term evolution may still be found for both 2D and 3D jets. In our theory, we assume clusters to be well separated and hydrodynamic interactions between them to be negligible. In particular, we ignore the fact that, rather than pinching off completely, small cylindrical threads of swimmers temporarily linger between clusters [Fig. 1(a)]. Indeed, such threads are expected to eventually be unstable to pearling like the initial jet, and not meaningfully alter the hydrodynamics due to their small size.

We now provide a summary of our results, while the details can be found in the specified Appendix sections. In what follows, we set the swimming speed to zero, as a finite value only rigidly translates the clusters upwards without changing their shape (since all swimmers are aligned).

A. Similarity solutions

We first show in Appendixes E 1 and E 2 that the clusters eventually stretch in a self-similar fashion (neglecting cluster-cluster interactions), attaining an oblate ellipsoidal shape in 3D and an elliptical shape in 2D. In the self-similar limit, independently of the initial shape, we find that the semimajor axes R_{3d} , R_{2d} of the 3D and 2D clusters eventually grow in time like

$$R_{3d}(t) \sim \left(\frac{9}{32} \frac{S\phi_0 V_0}{\mu V} \right)^{1/3} t^{1/3}, \quad (29a)$$

$$R_{2d}(t) \sim \left(\frac{S\phi_0 A_0}{\pi \mu V} \right)^{1/2} t^{1/2}, \quad (29b)$$

where V_0 is the initial cluster volume in 3D and A_0 is the initial cluster area in 2D. In both the 3D and the 2D geometry, clusters stretch perpendicularly to the z axis. The scalings in Eq. (29) are expected to hold as long as R_{3d} , R_{2d} are much smaller than the typical cluster-cluster separation, in each case giving a cut-off time of order ϕ_0^{-1} . The semiminor axes are found by imposing that the volume of the oblate ellipsoid (3D) and ellipse (2D) are V_0 and A_0 at all times, since clusters stretch under incompressible flow [Eq. (10)]. The semiminor axes therefore shrink like $t^{-2/3}$, $t^{-1/2}$ in the respective cases. The power laws in Eq. (29) may be rationalized by noting that a dipolar flow decays like $1/r^2$ in 3D, meaning that particle-particle separation grows like $\dot{r} \sim 1/r^2$, or $r \sim t^{1/3}$. Similarly, because the dipole flow decays like $1/r$ in 2D, we expect $\dot{r} \sim 1/r$, or $r \sim t^{1/2}$. Incidentally, the result in Eq. (29b) provides an asymptotic solution for the spreading of 2D pusher clusters [44], which stretch into ellipses along an axis perpendicular to that of puller clusters.

B. Exact solution for spherical and cylindrical clusters

Under the simplifying assumption that the initial cluster shape is a sphere (3D), or a circle (2D), we further show in Appendixes E 1 and E 2 that the cluster shape is *exactly* an oblate ellipsoid (3D) or an ellipse (2D) at all times. In the 3D setup, the time evolution of the semimajor axis, nondimensionalized by the initial value R_0 , is governed by

$$\frac{dR}{dt} = \frac{S\phi_0}{4\mu V} \frac{R^7}{(R^6 - 1)^2} \left[-3 + \frac{R^6 + 2}{(R^6 - 1)^{1/2}} \cos^{-1} \left(\frac{1}{R^3} \right) \right], \quad (30a)$$

$$R(0) = 1, \quad (30b)$$

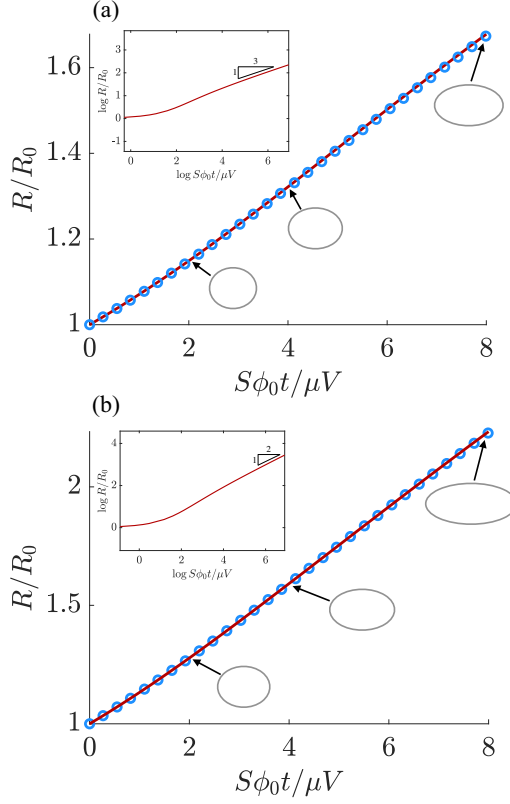


FIG. 5. Evolution of puller clusters with time. (a) An initially spherical cluster stretches exactly into an oblate ellipsoid of semimajor axis R . The solid red line represents the predicted evolution obtained by solving for the flow [i.e., Eqs. (30a) and (30b)]; the light blue circles represent numerical data (boundary integral method). Inset shows the long-term evolution, wherein the cluster stretches in a similarity solution with time dependence $R \sim t^{1/3}$, as predicted theoretically in Eq. (29a). (b) Corresponding evolution of a 2D cluster of pullers, which stretches into an elliptical cylinder. The red line is the numerical solution of Eqs. (31a) and (31b), while the light blue circles are numerical data. Inset: The cluster eventually reaches a similarity solution with $R \sim t^{1/2}$, as predicted in Eq. (29b). In both cases, clusters stretch perpendicularly to the axis of the original jet.

while in 2D it is given by

$$\frac{dR}{dt} = \frac{S\phi_0}{2\mu V} \frac{R^3}{(1+R^2)^2}, \quad (31a)$$

$$R(0) = 1. \quad (31b)$$

We can confirm the analytical findings through direct numerical simulations based on the integral solution of the Stokes equations [45,46] (details of the numerical schemes are provided in Appendixes E 5 a and E 5 b), as well as agent-based simulations of a 2D sheet of pullers (Sec. VII A). A summary of our results is shown in Fig. 5, where we compute the dimensionless cluster radius versus dimensionless time for the 3D [Fig. 5(a)] and 2D [Fig. 5(b)] systems. In each case, the solution of Eqs. (30) and (31) is compared with the values from the boundary integral method, showing excellent agreement. In particular, we visually demonstrate the transition between the initial-conditions-dependent evolution and the self-similar dynamics for $t \gg \mu V/S\phi_0$. We note that, as the shapes determined from the boundary integral method are subject to numerical errors,

these solutions are prone to developing a zigzag instability analogous to the one in Sec. IV (see Sec. VII B 3). From Eqs. (26) and (27) with $\xi = 1/2$ (the most unstable wave number), we know that this instability grows on a timescale $4e \times \mu V/S\phi_0$; stopping numerical integration at the earlier time $8 \times \mu V/S\phi_0$ (Fig. 5) therefore prevents this instability from developing.

C. Interactions between clusters

So far, we have considered the behavior of clusters in isolation, assuming cluster-cluster interactions to be negligible. We may now use the leading-order external flows, determined in Appendixes E 1 and E 2, to analyze cluster-cluster interactions, in the limit where clusters only interact in the far field (i.e., when the typical cluster size is much smaller than the typical separation length). In this case, because the leading-order external flow is the same as the (negative) perturbation flow of an oblate ellipsoid (3D) or an ellipse (2D) in strain flow, clusters interact as stresslets at leading order. In Appendixes E 3 a and E 3 b, we demonstrate that the stresslet strengths are given by

$$\mathbf{S} = SN(\mathbf{e}_z \mathbf{e}_z - \frac{1}{3} \mathbf{I}), \quad (3D) \quad (32a)$$

$$\mathbf{S} = S\tilde{N}(\mathbf{e}_z \mathbf{e}_z - \frac{1}{2} \mathbf{I}_2), \quad (2D) \quad (32b)$$

where $\mathbf{I}_2 = \text{diag}(1, 0, 1)$, N is the total number of swimmers inside the 3D cluster and \tilde{N} is the number per unit extent in the y direction inside the 2D cluster.

Remarkably, this leading-order flow does not depend on the clusters' elongation. Therefore, assuming the separation between clusters to be much larger than the typical cluster size, we expect clusters themselves to interact like a line of puller stresslets [36] of strength SN or $S\tilde{N}$, arranged along the z axis [Fig. 1(a)]. In particular, the spacing between the clusters is unstable, and we expect them to merge over time. Specifically, if λ is the typical cluster-cluster separation (on the order of the pearling wavelength), then the typical external velocity field felt by each cluster has typical size $SN/\mu\lambda^2$ in 3D and $S\tilde{N}/\mu\lambda$ in 2D, so that clusters are expected to merge on a timescale $\mu\lambda^3/SN$ in 3D and $\mu\lambda^2/S\tilde{N}$ in 2D.

D. Two-dimensional cluster rotation and the “V” instability

We have so far considered the dynamics of puller clusters extending perpendicularly to the alignment direction \mathbf{e}_z . A similar, but more general, calculation may be carried out when the major axis of a two-dimensional puller cluster is tilted at an angle $\alpha \neq 0$ relative to the x direction. As for the case $\alpha = 0$ (Sec. V B), we only summarize the main results of the computation, with further details explained in Appendix E 4.

In the idealized case where the cluster is initially an ellipse, we analytically show that its shape remains exactly elliptical at all times, while undergoing both stretching and rotation. Endowing the cluster with rotated coordinates (x', z') , and defining its semimajor and minor axes to be a and b , respectively [see Fig. 6(a)], the flow \mathbf{u} within the cluster takes the form

$$\mathbf{u} = E(x'\mathbf{e}'_x - z'\mathbf{e}'_z) + \Omega_1\left(\frac{x'}{a^2}\mathbf{e}'_z - \frac{z'}{b^2}\mathbf{e}'_x\right) + \Omega_2(x'\mathbf{e}'_z - z'\mathbf{e}'_x). \quad (33)$$

The three terms correspond, in order, to transverse straining motion, elliptical recirculation (“tread-milling”), and rigid-body rotation. Matching boundary stresses, the corresponding flow strengths can be found in terms of the cluster's tilt angle α [Fig. 6(a)]:

$$E = \frac{S\phi_0}{2\mu V} \frac{ab \cos(2\alpha)}{(a+b)^2}, \quad (34a)$$

$$\Omega_1 = \frac{S\phi_0}{2\mu V} \frac{a^2b^2(a^2+b^2)\sin(2\alpha)}{(a+b)^3(a-b)}, \quad (34b)$$

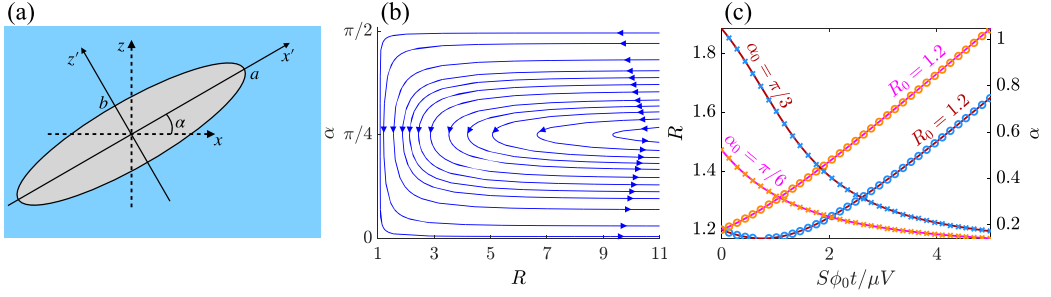


FIG. 6. Dynamics of tilted puller clusters. (a) Clusters are rotated ellipses with semimajor/minor axes a and b (respectively). Clusters are endowed with an (x', z') coordinate system rotated through an angle α from the horizontal. (b) Phase diagram of evolution of dimensionless semimajor axis R and angle α . (c) Representative trajectories for initial conditions: $R_0 = 1.2$ and $\alpha_0 = \pi/6$, $\alpha_0 = \pi/3$. Solid lines represent theoretical predictions from Eq. (35), while scatter plots represent numerical values obtained with the boundary-integral method in Appendix E 5 b.

$$\Omega_2 = -\frac{S\phi_0}{\mu V} \frac{a^2 b^2 \sin(2\alpha)}{(a+b)^3(a-b)}. \quad (34c)$$

Denoting by $\mathcal{A}_0 \equiv ab$ the constant cluster area, it is thus found that the dimensionless semimajor axis $R = \mathcal{A}_0^{-1/2} a$ and angle α obey the coupled evolution equations,

$$\frac{dR}{dt} = \frac{S\phi_0}{2\mu V} \frac{R^3 \cos(2\alpha)}{(R^2 + 1)^2}, \quad (35a)$$

$$\frac{d\alpha}{dt} = -\frac{S\phi_0}{\mu V} \frac{R^4 \sin(2\alpha)}{(R^2 + 1)^3(R^2 - 1)}. \quad (35b)$$

The initial conditions are of the form $\alpha(0) = \alpha_0$, $R(0) = R_0 > 1$ (as R_0 corresponds to the longer axis of the starting ellipse).

Assuming (without loss of generality) that $\alpha_0 \in [0, \pi/2]$, the phase portrait for both $R(t)$ and $\alpha(t)$ is plotted in Fig. 6(b), while representative trajectories are depicted in Fig. 6(c). We note the presence of constant-angle (equilibrium) solutions with $\alpha \equiv 0$ or $\alpha \equiv \pi/2$. Both of these regimes correspond to the cluster contracting along \mathbf{e}_z and expanding along \mathbf{e}_x , with late-time behaviors $R \sim t^{1/2}$, $R \sim t^{-1/2}$, respectively.

If, on the other hand, $\alpha_0 \in (0, \pi/2)$, then α decreases monotonically from its initial value, eventually approaching some limiting value α_∞ as $R \rightarrow \infty$. This limit be found by directly integrating Eq. (35):

$$\alpha_\infty = \frac{1}{2} \sin^{-1} \left(\frac{R_0^2 - 1}{R_0^2 + 1} \sin 2\alpha_0 \right). \quad (36)$$

Since $\alpha_\infty \in (0, \pi/4)$ for any initial α_0 , all cluster angles are eventually found in this range. Finally, the radial deformation is expected to appear slowest when $\alpha_\infty \sim \pi/4$, corresponding to $\alpha_0 \sim \pi/4$ and $R_0 \gg 1$. In other words, while no exact steady state exists for both R and α , clusters evolve the slowest when they are long and tilted at $\pm 45^\circ$, consistently with the “V” instability observed in Ref. [44] for elongating clusters of aligned active particles. We remark that, while the simulations in Ref. [44] involved pusher stresslets oriented along the x axis [see Fig. 6(a)], the argument in Sec. IV shows that this system evolves identically to a cluster of puller stresslets oriented along the z axis [Fig. 6(a)]. We finally remark that, at late times, specifically in the limit $t \gg \mu V / S\phi_0$, the radial

dynamics is expected to follow the self-similar behavior

$$R(t) \sim \left(\frac{S\phi_0 \cos 2\alpha_\infty}{\mu V} \right)^{1/2} t^{1/2}, \quad (37)$$

corresponding to the $R \gg 1$ limit of Eq. (35a). Eq. (37) generalizes Eq. (29b) to the case of a tilted cluster. A plot of the flows inside and outside a tilted 2D elliptical cluster is provided in Fig. 11(b), where we see good agreement with experimental measurements.

VI. LONG-TERM NONLINEAR EVOLUTION OF THE 3D HELICAL PUSHER INSTABILITY

We finally turn our attention to the long-term evolution of the 3D pusher jet. While we have established that the initially cylindrical jet buckles into a helical mode, the linearized theory cannot capture the evolution of the jet after the instability has fully developed. We may, however, obtain an approximate description of a buckled jet in the experimentally relevant limit of a slender structure, i.e., when the jet radius is much smaller than the buckling wavelength. We can once again ignore the swimming speed, which only results in a rigid translation of the jet.

A. Slender-body theory

While obtaining exact solutions outside the linear regime appears difficult, a considerable simplification is offered by the observation that the selected wavelength $\lambda^* \sim 9.8943 \times a$ is considerably larger than the radius of the jet. It therefore seems legitimate to approximate the flows associated with large zigzags via an asymptotic expansion in the small slenderness $a/\lambda^* \sim 0.1$.

Informally, while the ambient flow created by each section of the jet varies on a length scale a , the curvature of the jet only becomes apparent on a much larger length scale $L \sim \lambda^*$ [Fig. 7(a)]. The flow around the jet is therefore locally the same, with corrections of order a/L , as the flow around an infinite straight cylinder. At leading order in a/L , the slender jet therefore appears as a collection of noninteracting straight cylinders with different cross sections [Fig. 7(b)], each driving a flow via the active boundary stress $S\phi_0(\mathbf{e}_z \cdot \mathbf{n})\mathbf{e}_z/V$. We can determine the flow associated with each cylinder by solving Eqs. (14a)–(16c), while simultaneously identifying the local jet shape \mathcal{P} . In the framework of matched asymptotics, this leading-order flow in $\|\mathbf{x} - \mathbf{x}_0\| = \mathcal{O}(a)$, where \mathbf{x}_0 is the centerline point of interest, should then be matched onto the $\mathcal{O}(a/L)$ ambient flow generated by sections of the jet with $\|\mathbf{x} - \mathbf{x}_0\| \gg a$. In order to determine the leading-order inner solution, we endow the centerline $\mathbf{x}(s)$ of the jet (s being arclength) with a local orthonormal material frame $\{\mathbf{t}_1, \mathbf{t}_2, \mathbf{t}_3\}$, defined as [see Fig. 7(b)]

$$\mathbf{t}_1(s) = \sin \zeta(s) \cos \psi(s) \mathbf{e}_x + \sin \zeta(s) \sin \psi(s) \mathbf{e}_y - \cos \zeta(s) \mathbf{e}_z, \quad (38a)$$

$$\mathbf{t}_2(s) = -\sin \psi(s) \mathbf{e}_x + \cos \psi(s) \mathbf{e}_y, \quad (38b)$$

$$\mathbf{t}_3(s) = \cos \zeta(s) \cos \psi(s) \mathbf{e}_x + \cos \zeta(s) \sin \psi(s) \mathbf{e}_y + \sin \zeta(s) \mathbf{e}_z. \quad (38c)$$

Here $\mathbf{t}_3 = \mathbf{x}'(s)$ is the local unit tangent, \mathbf{t}_1 is a local unit normal, and \mathbf{t}_2 is the binormal parallel the xy plane. The angles ζ, ψ correspond to the local pitch (i.e., the slope relative to the xy plane) and yaw (i.e., the twist around the z axis), respectively [Figs. 7(b) and 7(c)]. Notice that $\{\mathbf{t}_1, \mathbf{t}_2, \mathbf{t}_3\}$ do not correspond to the usual Frenet frame. As the next step, we assume that the local cross section $\mathcal{C}(s)$ of the jet boundary, spanned by \mathbf{t}_1 and \mathbf{t}_2 , is at leading order an ellipse given by

$$\mathcal{C}(s) = \{\mathbf{x}(s) + a(s) \cos(\eta) \mathbf{t}_1(s) + b(s) \sin(\eta) \mathbf{t}_2(s) : 0 \leq \eta < 2\pi\}, \quad (39)$$

where $a, b > 0$ are the (unknown) semiaxes. We will later see that, at late times, $a > b$. Intuitively, the cross section at each point is a tilted ellipse such that the plane spanned by the surface normal \mathbf{t}_3 and the major axis $a\mathbf{t}_1$ is parallel to \mathbf{e}_z [see illustration in Figs. 7(b) and 7(c)]. The inner solution at each point $\mathbf{x}(s_0)$ is then the solution of Eqs. (14a)–(16c) with \mathcal{P} being an infinite elliptical cylinder with axis $\mathbf{x}(s_0) + s\mathbf{t}_1(s_0)$ ($-\infty < s < \infty$) and constant cross section $\mathcal{C}(s_0)$.

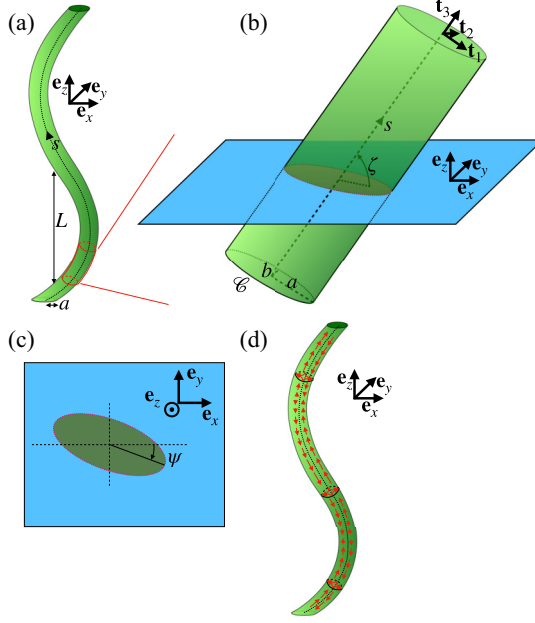


FIG. 7. Model of titled pusher jet. (a) The jet is assumed to be slender, i.e., its local radius a is much smaller than the length scale L from its curvature. (b) In this limit, the jet locally looks like an infinite straight cylinder, which we find to be elliptical in cross section. The local semimajor and minor axes are labeled a and b , respectively. The cylinder is endowed with a local material frame $\{\mathbf{t}_1, \mathbf{t}_2, \mathbf{t}_3\}$, with $\mathbf{t}_1, \mathbf{t}_2$ pointing along the semiaxes, and \mathbf{t}_3 aligned with the axis of the cylinder. The local pitch and yaw are denoted by ζ and ψ , respectively [with ψ defined as shown in (c)], and the cross-section boundary is $\mathcal{C}(s)$, with s being the axial arclength. (d) Schematic representation of the flow (red arrows) inside a three-dimensional buckled jet of pushers. The axial component of the pushing force drives an axial shear flow, while the transverse force component generates a straining flow which deforms the jet. The shearing flow is strongest when $\zeta = \pi/4$ or $\zeta = 3\pi/4$, and it vanishes when $\zeta = \pi/2$ (vertical sections). Arrow sizes are used solely to qualitatively illustrate the flow strength.

Defining local Cartesian coordinates $\mathbf{x} - \mathbf{x}(s_0) = x_1\mathbf{t}_1 + x_2\mathbf{t}_2 + x_3\mathbf{t}_3$, the local flow inside the jet associated with this configuration is assumed to be a combination of axial shear and cross-sectional strain [Fig. 7(d)]:

$$\mathbf{u} = \gamma x_1 \mathbf{t}_3 + E(x_1 \mathbf{t}_1 - x_2 \mathbf{t}_2), \quad (40a)$$

$$\boldsymbol{\sigma} = -p_0 \mathbf{I} + \gamma \mu (\mathbf{t}_1 \mathbf{t}_3 + \mathbf{t}_3 \mathbf{t}_1) + 2\mu E (\mathbf{t}_1 \mathbf{t}_1 - \mathbf{t}_2 \mathbf{t}_2). \quad (40b)$$

Imposing continuity of velocity and stresses at the jet boundary allows us to determine the straining rate E and the shearing rate γ as

$$E = -\frac{S\phi_0 \cos^2 \zeta}{2\mu V} \frac{\chi}{(1 + \chi)^2}, \quad (41a)$$

$$\gamma = \frac{S\phi_0 \sin 2\zeta}{2\mu V} \frac{\chi}{1 + \chi}, \quad (41b)$$

where $\chi = b/a$ is the aspect ratio (see details in Appendix F). Equation (41a) reflects the fact that the projection of the pusher dipole on the $\{\mathbf{t}_1, \mathbf{t}_3\}$ plane has magnitude $S \cos^2 \zeta$, resulting in an in-plane dynamics similar to that of stretching puller clusters (Sec. V). A jet of pushers ($S < 0$)

therefore stretches along \mathbf{t}_1 [Eq. (41a)]. The $(\mathbf{t}_1, \mathbf{t}_3)$ plane, in which extension occurs, corresponds to the plane slicing the jet in half and parallel to the z axis.

B. Evolution of the clusters

Our results indicate that, at leading order in a/L , a solution exists wherein the centerline of the jet is frozen in space, while the cross section deforms dynamically. Importantly, this does not contradict the shape evolution computed in our previous linear stability analysis (Sec. III), since leading-order slender-body theory is insensitive to deformations of order $\mathcal{O}(\varepsilon) \ll \mathcal{O}(a/L)$. Once the perturbation has fully developed, the small initial $\mathcal{O}(\varepsilon)$ perturbation is forgotten and our theory suggests the existence of a steady solution for the shape. Once the jet has reached a steady state, our analysis suggests that the structure is still highly dynamical: Cells are stirred by the shearing flow, which carries them in loops from peak to peak, where $\gamma = 0$ [Fig. 7(d)].

Our theory also predicts that each cross section $\mathcal{C}(s)$ progressively deforms into a slender ellipse of constant area under the transverse straining flow. Specifically, if $R(t)$ is the local semimajor axis, nondimensionalized by the initial value [i.e., $R(t) = a(t)/a(0)$], then Eq. (41a) implies that

$$\frac{dR}{dt} = -\frac{S\phi_0 \cos^2 \zeta}{2\mu V} \frac{R^3}{(1 + R^2)^2}. \quad (42)$$

At large times, Eq. (42) indicates that $\dot{R} \sim R^{-1}$, or $R \sim t^{1/2}$. Therefore, the local cross section becomes increasingly stretched over time.

VII. COMPARISON WITH EXPERIMENTS AND SIMULATIONS

In order to validate the theory developed in this paper, in this section we compare our predictions with our experiments and with numerical simulations. A detailed comparison of the predicted wavelengths and growth rates is carried out in Ref. [37], to which the reader is referred for further details. Here our main focus will instead be on validating the predicted long-term dynamics of each instability.

A. Comparison with numerical simulations

1. Numerical setup and method

We carried out agent-based simulations for the 2D setup described in Sec. IV, as well as the 3D setup in Sec. III. In the two-dimensional case [Figs. 9(a), 9(b), and 9(d)], active particles of radius a_s were seeded uniformly at random in the domain $-a < x < a$. The particles were taken to be squirmers with a prescribed surface slip velocity

$$\mathbf{u}_s = \frac{3}{2}U\beta \sin \theta \cos \theta \mathbf{e}_\theta \quad (43)$$

(U being a typical velocity) in body-fixed spherical polar coordinates centered around the swimming direction \mathbf{p} . Because the activation has front-back reflectional symmetry, the swimming speed of such squirmers is $U_s = 0$, making them “shakers.” This choice made the jet structure more robust, and allowed the instabilities to be tracked for longer; furthermore, from our theoretical analysis, we do not expect the swimming speed to change our conclusions when the swimming direction is held fixed. A shaker endowed with slip velocity (43) exerts a stresslet on the fluid of scalar magnitude [47]

$$S = 6\pi\beta\mu a_s^2 U. \quad (44)$$

In 2D simulations, we always took $\beta > 0$ (so that $S > 0$, appropriate for *C. reinhardtii* algae). In addition, particles were assumed to reorient in response to an aligning torque, which, as we argued in Sec. II, does not affect the leading-order dynamics and is thus an appropriate mechanism for simulating experiments with phototaxis [37]. To simulate the pearling instability [Figs. 9(a) and

9(d)], the restoring torque was taken to be axial, with

$$\mathbf{G} = G_{\text{bh}} \mu a_s^2 U \mathbf{p} \times \mathbf{e}_z, \quad (45)$$

and dimensionless strength $G_{\text{bh}} > 0$. Conversely, to reproduce the zigzag instability [Figs. 9(b) and 9(d)] observed experimentally with pullers [37], active particles were instead rotated towards the axis of the jet ($x = 0$) by means of a torque

$$\mathbf{G} = -\mu a_s^2 U G_{\text{bh}} \text{sgn}(x) \mathbf{p} \times \mathbf{e}_x, \quad (46)$$

where $\text{sgn}(x)$ is the sign function. From Sec. IV, we thus infer that this sheet should have the same evolution as a sheet of axially oriented pushers of strength $-S$.

The motion of the squirmers in response to the collective flow generated by the active stresses was computed with the aid of Stokesian dynamics [48], supplemented with periodic boundary conditions for the flow in the y and z directions. Such boundary conditions were implemented purely to allow for numerical resolution and were chosen to approximate an unbounded domain. In our simulations, we took the 2D jet to occupy the domain $96.5a_s < x < 103.5a_s$, $0 < y < 20a_s$, $0 < z < 200a_s$, while the box was instead taken to be $0 < x < 200a_s$, $0 < y < 20a_s$, $0 < z < 200a_s$. For the chosen volume fraction, the average interswimmer distance at $t = 0$ was about $2.7a_s$. In order to keep the jet coherent, the reorientation timescale B (estimated by balancing the applied torque with the torque on a rotating rigid sphere)

$$B \sim \frac{a_s}{G_{\text{bh}} U} \quad (47)$$

was always taken to be much smaller than the instability timescale T [Eqs. (23), (26), and (27)]

$$T \sim \frac{\mu V}{S \phi_0} \sim \frac{a_s}{|\beta| U \phi_0}. \quad (48)$$

This was achieved by choosing $G_{\text{bh}} \gg |\beta| \phi_0$. In typical simulations $G_{\text{bh}} \sim 100$, $\phi_0 \sim 0.1$, $|\beta| \sim 1$, so reorientation was essentially instantaneous on the timescale of the flow.

2. Comparison with theory at early and late times

Numerical simulations of axial and rotated puller sheets exhibited the expected pearling/zigzag instabilities (respectively), with wavelengths and timescales compatible with the theoretical predictions in Sec. IV. The temporal evolution of the sheet is seen to scale linearly with β , as demonstrated by the collapse of the growth curves in Figs. 9(a) and 9(b) when plotted against the dimensionless time $t^* = 6\pi\beta\phi U t/a_s$. Exponential fitting of the growth curves in Figs. 9(a) and 9(b) provides the estimates $r/a \sim 1 + 0.37 \times \exp(0.029 \times t^*)$ (r being the average position $|x|$ of the 15% outermost swimmers) for axial pullers [Fig. 9(a)], and $r/a \sim 1 + 0.35 \times \exp(0.019 \times t^*)$ for rotated pullers [Fig. 9(b)]. The number of significant figures in the fitted values reflects the corresponding 95% confidence intervals. The dimensionless growth rates extracted from simulations may now be compared with Eqs. (26) and (27) for $\xi = 1/2$ (the most unstable wave number). After nondimensionalizing the corresponding growth rates by $6\pi\beta\phi U/a_s$, we find that, for both instabilities, $s^* = 3/(16\pi e) \sim 0.0220$, which closely resembles the numerical estimates. The fitted values of ε are instead not as significant, as the initial perturbation is inherently random.

The long-term behavior of the puller sheet in Fig. 9(a) was further investigated. As clusters stretch thin, the zigzag instability predicted in Sec. IV is indeed observed [Fig. 8(a)], and the resulting clusters attain a shape reminiscent of the “V” instability (Sec. VD, [44]). Before this happens, the evolution of the clusters is approximately given by Eq. (29b). In particular, the numerical long-term growth can be fitted by $r/a \sim 0.578 \times (t^* - 49)^{1/2}$ [Fig. 9(a)], suggesting that the sheet pinches off at $t^* \sim 49$, consistently with the theoretical dimensionless instability timescale $1/\sigma^* \sim 45.5452$. We remark that, since the clusters are not precisely ellipses to start with, the exact solutions derived in Secs. VB and VD are only in qualitative agreement with the numerical clusters [Fig. 8(a)]. On the

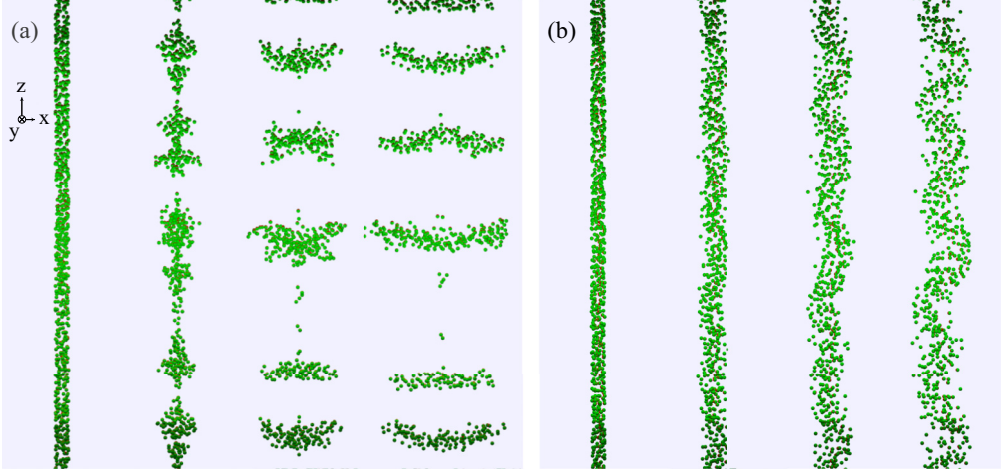


FIG. 8. Numerical realization of the phenomena captured experimentally in Fig. 1. (a) A sheet of squirmers, subject to an external torque aligning swimmers along the sheet axis, breaks up into clusters, which stretch horizontally over time before developing a “V”-shaped instability. (b) When squirmers are subject to a torque that tries to rotate them towards the axis of the sheet, the zigzag instability emerges instead.

other hand, as cluster continue to stretch, they transition to the self-similar behaviors from Secs. V A and V D, since a thin cluster has no memory of its initial shape.

The long-term evolution of the pusher instability was further investigated in Fig. 9(c) by considering a three-dimensional setup similar to the one studied theoretically in Secs. III and VI. This time, spherical pushers were initially distributed uniformly at random inside a cylindrical domain $r \leq 3.5a_s$ [Fig. 9(c)], and an axial torque [Eq. (45)] was applied to maintain their axial orientation. The box size was in this case taken to be $-200a_s < x, y < 200a_s$, $-100a_s < z < 100a_s$, and the average interswimmer distance at $t = 0$ was about $2.3a_s$. After the jet buckled, we proceeded to track the displacement of the x and y coordinates of the jet centerline, calculated by breaking up the jet into sections and calculating the average swimmer position within each section [Fig. 9(c)]. This revealed helical buckling, with $x(z)$ and $y(z)$ showing out-of-phase periodic variations. The instability wavelengths measured in Fig. 9(c) suggest $8 \leq \lambda/a \leq 10$, consistently with our theoretical prediction $\lambda/a \sim 9.8943$ derived in Sec. III D. We further show in Fig. 9(c) that the shape of the jet does not change meaningfully over time, consistently with the slender-body analysis in Sec. VI.

Finally, in Fig. 9(d) we show the measured wavelength for a sheet of axial and rotated pullers. Numerical results are in very good agreement with the theoretical prediction $\lambda/a \sim 4\pi$, derived in Sec. IV.

B. Comparison with experiments

We now compare the predictions of our theory with the experimental data from Ref. [37]. As a reminder, in our experiments we employ a strain of *C. reinhardtii* (CC125) in photophobic conditions to study both instability types. The puller instability was obtained when cells were aligned with the jet axis while, in order to generate the instability for pushers, algae were oriented perpendicularly to the jet axis by means of strong parallel arrays of LEDs. By doing so, the flow field around each swimmer resembled that of a pusher oriented along the vertical axis of the jet.

1. Parameters

In our experiments, due to the illumination geometry and the presence of the tank, the geometry of the jet is halfway between the cylindrical and sheetlike cases in Fig. 2. Specifically, the jet takes the shape of a flattened cylinder, with a width of about 100–200 μm in the x direction and about

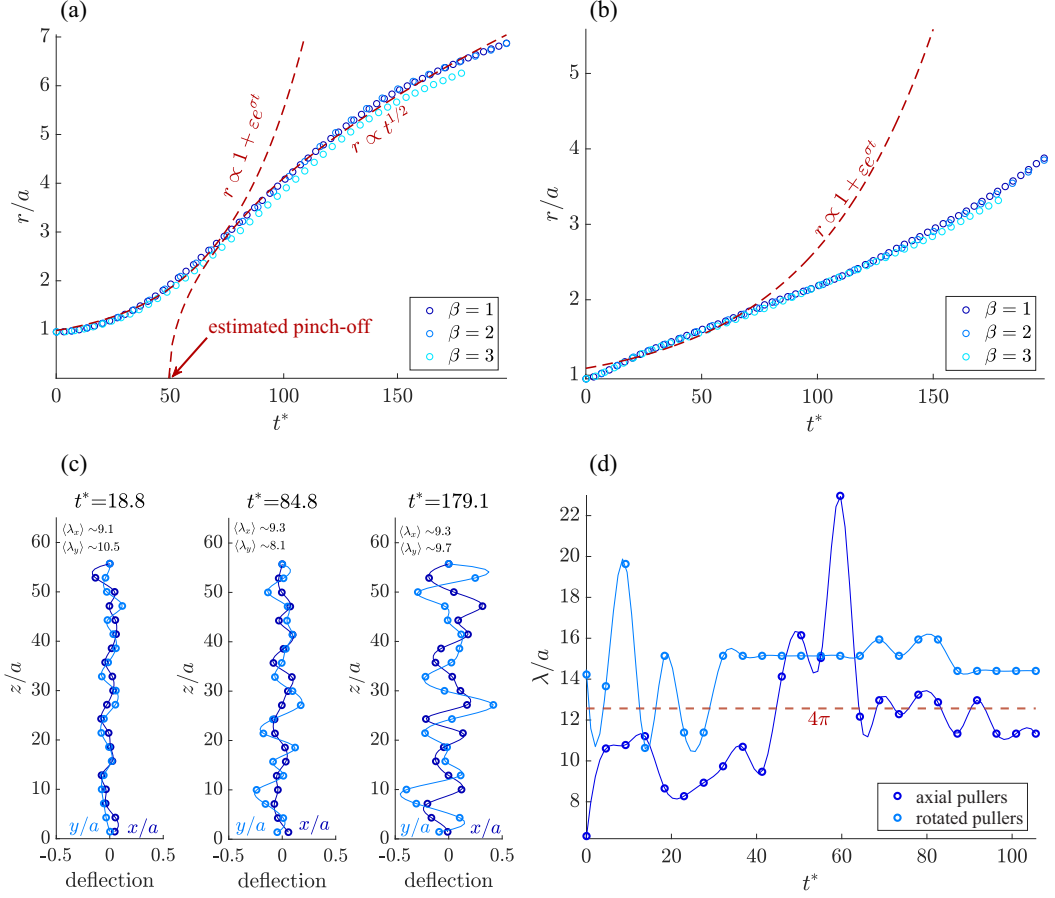


FIG. 9. Summary of results of numerical simulations. (a) Time evolution of a two-dimensional sheet of axial pullers. Circles represent the axial deflection in the x direction (numerical data) as a function of dimensionless time $t^* = 6\pi\beta\phi Ut/a_s$ for various values of β , showing collapse of the data. The dimensionless axial deflection was computed by averaging $|x|/a$ over the 15% outermost swimmers. We fitted the early-time behavior with $r/a \sim 1 + \varepsilon \exp(\sigma t)$ and the late-time with $r/a \sim p(t - q)^{1/2}$ (see Sec. V). (b) Similar analysis as (a), but for a sheet of rotated pullers; curves once again collapse neatly for varying β . (c) Time evolution of a cylindrical jet of axial pushers. The jet was divided into vertical sections, and the average x and y positions of the swimmers in each section were computed (circles; solid lines serve as guides for the eye). When plotted again the section-averaged z , data show that the jet buckles into a helical mode. For each of $x(z)$, $y(z)$, time-dependent wavelengths λ_x , λ_y were estimated as the average distance between local maxima of the corresponding curves. (d) Evolution of the instability wavelength for a sheet of axial and rotated pullers. The wavelength was computed from the discrete Fourier transform of the swimmers' axial displacement. Numerical data (circles), show that $\lambda/a \sim 4\pi$, in agreement with the theory (see Sec. IV). Solid lines serve as guides for the eye.

50 μm in the y direction [37,49]. We thus expect the dynamics to be a hybrid of the limit cases discussed in Sec. III (cylindrical geometry) and Sec. IV (sheetlike geometry). The experimental jet satisfies the fast-reorientation limit detailed in Sec. IIB, given the typical experimental values $B \sim 1$ s, $T \sim 10$ s [37]. Likewise, the persistent sharp drop in concentration outside the jet [37] indicates that the Péclet number is large enough for the zero-diffusion approximation in Sec. IIB to be valid. On the other hand, by virtue of the mechanism for jet formation, the experimental jets are highly concentrated ($\phi \sim 0.5$ for the zigzag instability, $\phi \sim 0.2$ for the pearling instability).

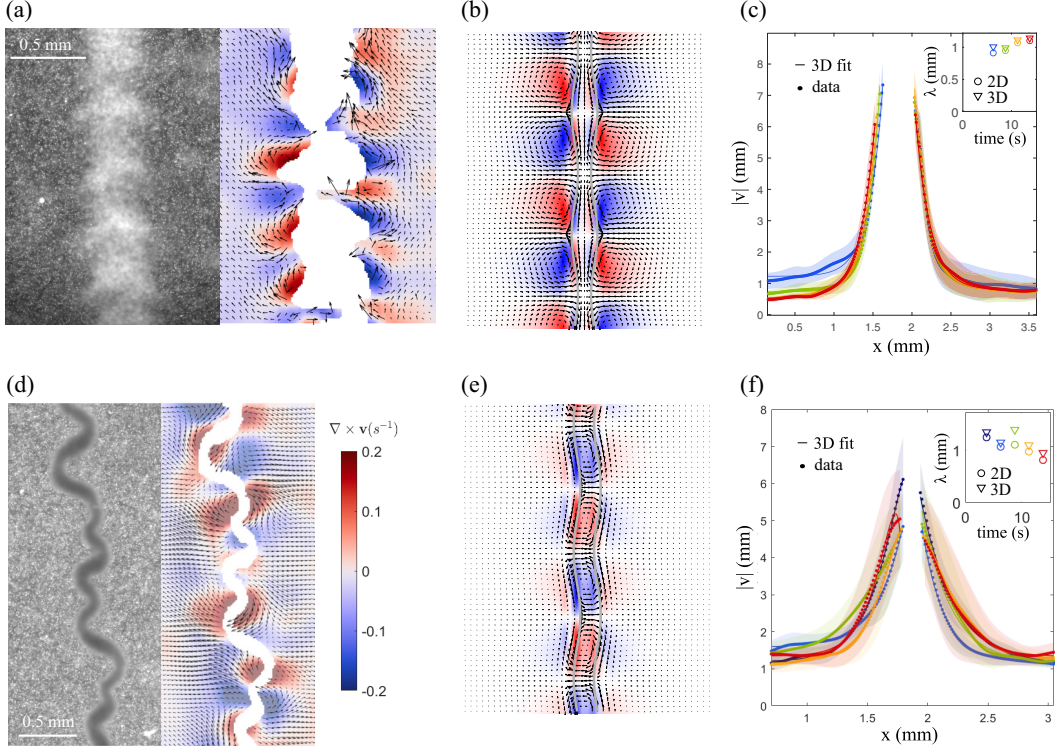


FIG. 10. Comparison of the flow structure around the jet. [(a) and (d)] Dark-field images of the jet of pullers (a) and rotated pullers (d) (left), along with PIV in the laboratory frame, with background color showing the out-of-plane component of the vorticity [right, same colourbar for (a) and (d)]. [(b) and (e)] Theoretical predictions for the flow direction and vorticity for the most unstable mode of a 3D jet of pushers and pullers, respectively. The vorticity fields near the jets match the ones in the PIV images (a) and (d). [(c) and (f)] Flow magnitude away from the jets at different times. Solid lines indicate fits with the three-dimensional decay rate $a(x - x_0)^{1/2} \exp[-k(x - x_0)] + d$, with a , x_0 , k , and d as free fitting parameters. Insets show the wavelength $2\pi/k$ obtained by fitting the 2D and 3D model to the experimental data.

As such, Eqs. (23), (26), and (27) provide upper bounds for the experimental growth rates, rather than precise estimates, as expected from the extra resistance added by particle-particle interactions. Indeed, further numerical simulations with a more concentrated jet than in Sec. VII A ($\phi_0 = 0.124$ instead of $\phi_0 = 0.07$, not shown) confirm that continuum theory overestimates the growth rate in the nondilute case.

Despite being well outside the dilute limit assumed in the theoretical framework, the experiments are nonetheless well described by both the 3D and 2D models, which correctly predict the type of instability and the characteristic wavelengths for axial and rotated pullers. This is likely because the instability wavelengths only depend weakly on the concentration. We refer the reader to the joint paper [37] for a full quantitative comparison of the initial instability dynamics; in what follows, we focus on the flows associated with the onset of each instability, as well as the long-term evolution.

2. Flow field at the onset of the instability

In Fig. 10 we show a comparison between the theoretical flow fields derived from Eqs. (B8a), (B8b), (B9), (B13a), (B13b), and (B14) (derivation in Appendix B), and the experimental measurements (See Supplemental Material Movies S1 and S2 [50]). We measured the fluid flow created

by the cells by particle image velocimetry (PIV) analysis of suspensions laden with passive tracer particles. We used polystyrene beads of 2 μm diameter as tracers. Movies were recorded under the microscope at 8 fps, using the sources driving the instability to achieve darkfield illumination. As we needed to distinguish algae from tracers to measure the flows, the exposure time was chosen high enough to blur the fast-swimming algae but low enough to keep the much slower beads crisp [Figs. 10(a) and 10(d)]. This allowed us to simultaneously track the jet destabilization (for which single-cell resolution is not necessary), and the flow fields. We then used Matlab's PIVlab, after running our images through a spatial band-pass filter to ensure only the beads' movements were taken into account.

We see from Fig. 10 that our model quantitatively agrees with the experiments in terms of both the flow circulation [Figs. 10(a) and 10(d) versus Figs. 10(b) and 10(e)], as well as the flow decay rate [Figs. 10(c) and 10(f)]. Specifically, from the results in Eqs. (B8a), (B8b), and (B9) for the external flow (Appendix B), we expect the flow field around a 3D jet to have a characteristic decay rate $\|\mathbf{u}_1^+\|^{(3D)} \sim rK_n(kr) \sim r^{1/2} \exp(-kr)$, which agrees very well with the data in Figs. 10(c) and 10(f). Similarly, the flow around a 2D jet is expected to decay like $\|\mathbf{u}_1^+\|^{(2D)} \sim x e^{-kx}$ [see Eqs. (D8a) and (D8b) in Appendix D] which also matches the flow data reasonably well, with fitted wavelength $2\pi/k$ comparable to the one obtained from the 3D fit. This reflects the fact that the geometry of the jet is a hybrid between our 3D and 2D setups.

3. Long-term evolutions of clusters and zigzags

We next set out to validate our theoretical predictions for the long-term evolutions of the instabilities. Visual comparison of the theoretical and experimental data is provided in Fig. 11. The expected elliptical cluster shape (Sec. VB) after pinch-off is in qualitative agreement with the experiments [Fig. 1(a)]. After ~ 1 min, the clusters destabilized into the “V” shape [see Fig. 1(a) and 11(c)] already shown in simulations [Fig. 8(a)]. The tilted clusters resulting from this instability are nearly elliptical in shape, in agreement with Sec. VD. This secondary instability can also be understood purely in terms of hydrodynamic interactions: from Sec. IV, we know that the flow within a stretching two-dimensional cluster is mathematically identical whether the swimmers are pullers oriented along the z axis, or pushers oriented along the x axis. Therefore, a spreading puller cluster behaves like a pusher jet oriented along the x axis. As such, two-dimensional puller clusters are subject to the zigzag instability (Sec. IV), which becomes apparent as soon as the major axis of the cluster is on the order of the wavelength $\lambda_{2D}^* = 4\pi w$ (w being the minor axis of the cluster). A single wavelength develops, giving the droplets their final characteristic “moustache” shape. These structures are stable and highly dynamic, with cells circulating in vortices over hundreds of micrometers [Fig. 11(c)]. Such stability, as well as the presence of the treadmilling flow [Fig. 11(a) and especially Fig. 11(c)], match the steady-state predictions from Sec. VD [Fig. 11(b)].

Remarkably, as shown in Ref. [44], a strongly aligned active suspension of microswimmers exhibits symmetries that restrict the allowed distribution of particles. In particular, the striking macroscopic “V” structures observed in experiments can be understood through a Hamiltonian formalism. The Hamiltonian for such a system is notably scale invariant and symmetric with respect to $\pm 45^\circ$, leading to lines of particles at angles $\pm 45^\circ$ —the same result we obtained through our flow calculation.

Furthermore, measured cluster aspect ratios [Fig. 11(d)] appear to decay at an average rate $\mathcal{O}(t^{-1})$, even though the data show high variability. This is in agreement with our theory (Sec. VA), predicting the aspect ratio to decay like t^{-1} in both 3D and 2D. The experimental variability is likely a consequence of noise, as well as interactions between the clusters, since the clusters are not isolated as assumed by the analytical prediction.

Finally, we consider the late-time evolution of the zigzags. As predicted by the theory (Sec. VI), the amplitude of the zigzags is seen to rapidly stabilize after the initial exponential growth [37] [Fig. 11(e)]. The theoretical flow, approximately consisting of a superposition of axial shear and transverse strain [Fig. 11(g)], agrees well with the detailed measurements in Fig. 11(e). Because

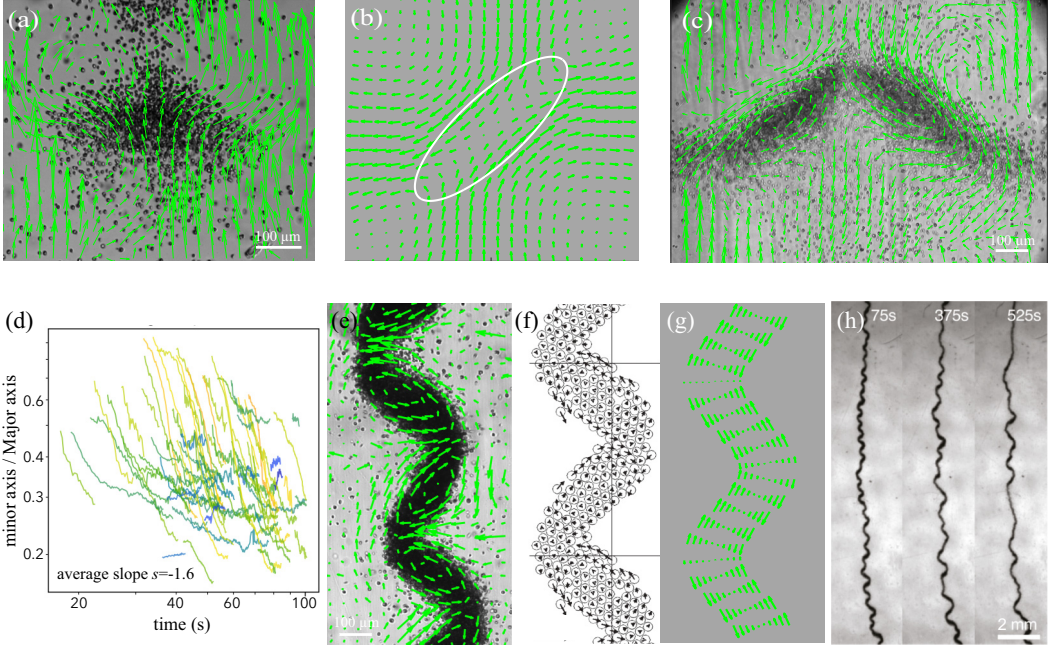


FIG. 11. Evolution of clusters and zigzags at large times. (a) Cell displacement field inside a puller cluster after the instability has first developed, highlighting strainlike flow inside the cluster and stressletlike flow outside (PIV on the cells in the reference frame of the cluster; the background flow corresponds to the global velocity of the cluster. Top view, light coming from the top of the image). (b) Theoretical flow field for a 2D puller cluster tilted at 45° (Sec. VD). (c) Cell displacement field in the final “V”-shaped cluster (PIV on the cells in the comoving frame, light coming from the top of the image). (d) Time evolution of experimental cluster aspect ratio. The color encodes the slope of the curves (yellow to blue). (e) Cell displacement field inside a jet of rotated pullers after the instability has first developed. (f) Same, numerics [2]. (g) Theoretical flow inside 3D zigzags at late times, consisting of axial shear and transverse strain. (h) Experiments showing coarsening of zigzag wavelength on the timescale of 5–10 min.

the shape evolution is slower where the jet is nearly vertical [i.e., $\cos \zeta \sim 0$ in Eq. (42)], we expect a less wavy jet to stay unchanged for longer. This is reflected in our experiments, where shape deformations lead to mergers of the zigzags, producing a slowly evolving structure with large wavelength [Fig. 11(h)]. The experimental jet is seen to slowly evolve over a period of minutes [Fig. 11(h)]. Such a large timescale is justified by Eq. (42), wherein $\cos^2 \zeta \ll 1$ for a nearly vertical jet ($\zeta \sim \pi/2$). For instance, taking $\cos \zeta \sim a/\lambda^* \sim 0.1$, the helical mode evolves on a timescale 100 times longer than the instability timescale. For an instability timescale of about 10 s, it would thus take on the order of 10^3 s (~ 15 min) to observe any significant changes [Fig. 11(h)].

4. Microscopic origin of an effective stresslet strength depending on light intensity

The driving force behind the instabilities (and the main parameter of the model) is the stresslet exerted by the cells on the fluid. In the experiments, however, the growth of the instabilities was controlled by the intensity of the axial (for clusters) or side (for zigzags) LEDs [37]. In order to rationalize the experimentally measured growth rates at different light intensities in the framework of the model, we investigated how cell swimming was related to the light intensity. To do so, we measured the trajectories of dilute suspensions of algae at different light intensities, under the same illumination geometries as Fig. 1 in Ref. [37]. The resulting swimming angle distributions were seemingly Gaussian, which allowed us to extract their standard deviation $d\theta(I)$, capturing

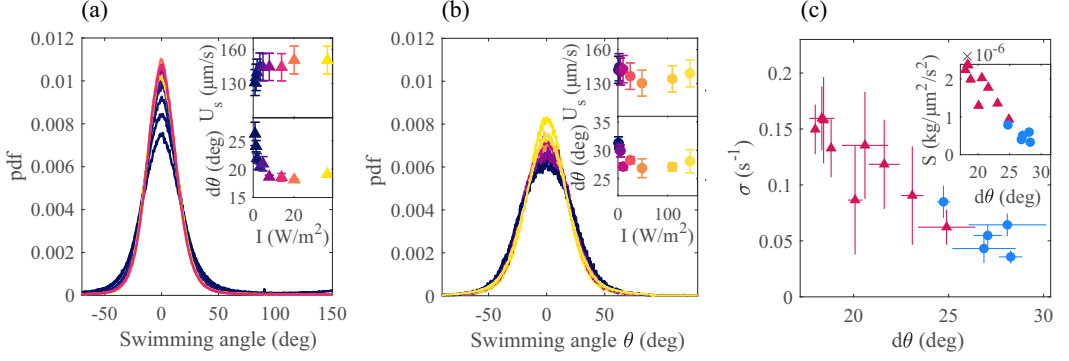


FIG. 12. Instantaneous swimming angle distributions of algae at the light intensities used in the macroscopic experiments. (a) zigzags setting with light coming from one side LED array, (b) pearling setting with a single collimated LED. Insets: angular dispersion $d\theta$, extracted from a Gaussian fit, and average swimming speed U_s vs light intensity. Colors correspond to light intensity. (c) The growth rates σ of the pearling (blue circles) and zigzags (red triangles) instabilities decrease with the angular swimming dispersion $d\theta$ of the cells. For each data point, σ and $d\theta$ were independently measured at a given light intensity. Inset: effective stresslets S_{eff} extracted from the growth rates using the 3D model with $\phi_0^{\text{zigzag}} = 0.5$ and $\phi_0^{\text{pearling}} = 0.2$.

the angular swimming dispersion around the light's main direction at a given intensity [Figs. 12(a) and 12(b)]. Importantly, the observably large spread of the distributions were mainly due to the cells' helical trajectories [51]. In both settings, cells followed the light direction more consistently as the intensity was increased. The algae swimming speed U_s also slightly changed with I [insets of Figs. 12(a) and 12(b)]. From the measured dependence of the instability growth rates on the angular dispersion $d\theta$ [Fig. 12(c)], we could estimate a corresponding “effective stresslet” from the theoretical predictions $\sigma_{3D}^{\text{pearling}} \sim 0.097 \times \frac{|S|\phi_0}{\mu V}$ and $\sigma_{3D}^{\text{zigzag}} \sim 0.024 \times \frac{|S|\phi_0}{\mu V}$ (Sec. III D), with the experimental values $\phi_0^{\text{pearling}} = 0.2$ and $\phi_0^{\text{zigzag}} = 0.5$. Remarkably, the estimates all fell on the same curve [inset of Fig. 12(c)], suggesting that the growth rate is indeed well described by our model, with S replaced by an effective stresslet $S_{\text{eff}}(d\theta)$. The magnitude of this effective stresslet decreased significantly as the angular dispersion $d\theta$ increased, which could not be justified solely in terms of the small change in swimming speed with light intensity. We instead propose that, when cells wobble around their main swimming direction, their average stresslet is smaller than when they swim along straight paths.

VIII. CONCLUSION

In this paper, we employed a coarse-grained continuum theory to investigate the shape instabilities of jets and sheets of active swimmers. Taken together, our results describe several geometric features of the invasion of clear fluid by a strongly aligned active suspension [52]. In Sec. II, we derived continuum equations for the evolution of coherent active structures, under the assumptions of negligible diffusion and a constant swimming direction. We then conducted a linear stability analysis of the shape of 3D jets (Sec. III), and 2D sheets (Sec. IV). We recovered the pearling instability for pullers and the helical/zigzag instability for pushers, and predicted observable features of such instabilities, such as the growth rates and wavelengths (the comparison of our predictions with experiments is detailed in our companion paper [37]). We then extended our continuum theory to study the long-term evolution of a puller cluster both in a 3D and in a 2D setup (Sec. V). We recovered exact solutions for the evolution of a spherical or cylindrical cluster, and derived universal long-term similarity solutions in the two cases. In particular, the scalings $r \sim t^{1/3}$ in 3D and $r \sim t^{1/2}$ in 2D reflected the underlying dipolar flows. We finally employed slender-body theory to derive approximate equations for the evolution of the 3D zigzags (Sec. VI), showing that, while the pusher

jet eventually stops buckling, its features continue evolving. We correctly predicted the flow inside the buckled jet and the timescales for wavelength coarsening, elucidating the underlying mechanism. We finished by comparing our results with direct numerical simulations (Sec. VII A) and experiments (Sec. VII B), recovering good agreement, both in terms of the instability wavelengths and growth rates, as well as the measured ambient flows. Our nonlinear theory quantitatively captured the stretching of puller clusters, and predicted the coarsening of three-dimensional zigzags as well as the corresponding timescale.

As shown experimentally in Ref. [37], our analysis confirms that the active stresses generated by microorganisms are sufficient to produce instabilities in coherently structured active jets. These instabilities are observed for both pusher and puller microorganisms. The nature of the flows driving the instabilities reflected the small-scale dipolar flows. Pullers tend to drive extensional flow perpendicular to their swimming direction (Sec. V), while pushers stretch coherent structures along their swimming direction (Sec. VI). Our analysis also revealed surprising self-similarities in the breakup of a puller jet, with aligned clusters driving a flow qualitatively identical to that of individual swimmers (Sec. VC).

Theoretically, a detailed investigation of the dynamics was possible thanks to the approximations of perfect alignment between the swimmers and the external light ($\mathbf{p} \equiv \mathbf{e}_z$), and of zero diffusion. It will be interesting to generalize these results to allow for rotating swimmers or a small diffusive boundary layer outside the jet (i.e., a finite Péclet number). While not necessary to recover the leading-order dynamics, diffusion is unavoidable in biological systems, and should therefore be accounted for in a more realistic model. One could also allow for a position-dependent reorientation speed, in order to model shadowing in the case of phototaxis: In experiments, cells in the middle of the jet do not receive much light, and their orientations are mostly incoherent.

Overall, this work highlights the richness and physical significance of aligned active suspensions, and we hope our study paves the way for further research on both theoretical and experimental levels.

ACKNOWLEDGMENTS

We thank Weida Liao for useful feedback. This work was partly funded by EPSRC (scholarship to MV) and supported through the Junior Research Chair Programme (ANR-10-LABX-0010/ANR-10-IDEX-0001-02 PSL; R.J.) and an ED-PIF doctoral fellowship (I.E.). T.I. is supported by JSPS KAKENHI (Grants No. 21H04999 and No. 21H05308).

DATA AVAILABILITY

The data that support the findings of this article are openly available [53].

APPENDIX A: DERIVATION OF CONTINUUM EQUATIONS

In this first Appendix, we provide two derivations of Eqs. (7a) through (9b) for the jet. In Appendix A 1, we show how to reconcile the sharp jet boundary with the requirement of statistical homogeneity [39]. In Appendix A 2, we recover Eqs. (7a) through (9b) from superposing the stresslet flows created by individual swimmers.

1. Solution from matched asymptotics

In this subsection, we aim to justify the assumption of a discontinuous concentration at the jet boundary, which may appear, at first, at odds with the implicit assumption of statistical homogeneity needed to identify $S(p_i p_j - \delta_{ij}/3)$ with the particle stress [Eq. (4)] [39]. More precisely, this step requires a separation of length scales between the particle size a_s and the local suspension length scale L (defined by $\nabla_x \phi \sim \phi/L$), such that there exists an intermediate length scale ℓ with

$$a_s \ll \ell \ll L. \quad (\text{A1})$$

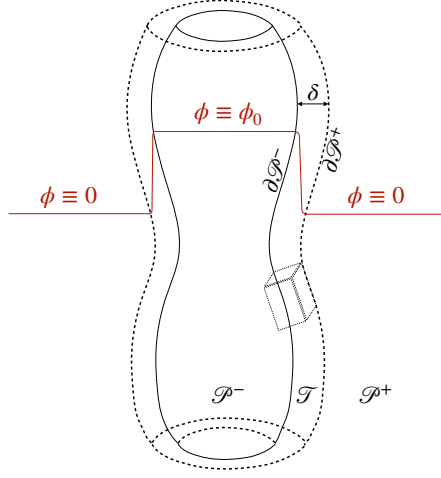


FIG. 13. Sketch of the smooth jet: the concentration ϕ varies smoothly between two constant values over a transition region \mathcal{T} of typical width δ . The inner and outer regions are denoted \mathcal{P}^- and \mathcal{P}^+ , with respective boundaries $\partial \mathcal{P}^-$ and $\partial \mathcal{P}^+$.

In other words, we should be able to find a volume around each particle containing many swimmers, and where the particle volume fraction does not change significantly. This condition is not satisfied in the presence of a step in the concentration, since, by definition, there is going to be an outermost particle beyond which the volume fraction drops discontinuously.

To address this issue, we interpret the step in the concentration as approximating a smoothly varying concentration field $\phi(\mathbf{x}, t)$, for which statistical homogeneity holds. At any point in time, the concentration is defined to be constant ($\phi \equiv \phi_0$) in the jet volume (which we henceforth denote \mathcal{P}^- , similarly to Sec. II D), and sharply decaying to zero on some length scale δ outside of \mathcal{P}^- . We let \mathcal{T} be the transition region where the concentration changes rapidly, and \mathcal{P}^+ be the region of space where the particle concentration is zero. We denote the boundaries of these two regions by $\partial \mathcal{P}^-$, $\partial \mathcal{P}^+$. These are assumed to be close to each other in the sense that there exists a continuous one-to-one mapping $\chi : \partial \mathcal{P}^- \rightarrow \partial \mathcal{P}^+$ such that $\|\mathbf{x} - \chi(\mathbf{x})\| \leq \delta$ for each $\mathbf{x} \in \partial \mathcal{P}^-$. A sketch of the jet is provided in Fig. 13. Such a jet is within the continuum limit as long as the swimmers are sufficiently small, i.e., as long as

$$a_s \ll \ell \ll \delta. \quad (\text{A2})$$

Assuming that the swimming direction is clamped, with $\mathbf{p} \equiv \mathbf{e}_z$, the particle stress may then be coarse-grained into an active stress tensor

$$\Sigma_{ij} = -q\delta_{ij} + \mu \left(\frac{\partial u_i}{\partial x_j} + \frac{\partial u_j}{\partial x_i} \right) + \frac{S\phi}{V} p_i p_j. \quad (\text{A3})$$

For convenience, we denote the Newtonian part of the stress by σ_{ij} , with

$$\sigma_{ij} = -q\delta_{ij} + \mu \left(\frac{\partial u_i}{\partial x_j} + \frac{\partial u_j}{\partial x_i} \right). \quad (\text{A4})$$

The conditions of stress-balance, incompressibility, and swimmer conservation take the form

$$\partial_j \Sigma_{ij} = 0, \quad (\text{A5a})$$

$$\partial_i u_i = 0, \quad (\text{A5b})$$

$$\frac{\partial \phi}{\partial t} + (\mathbf{u} + U_s \mathbf{e}_z) \cdot \nabla \phi = 0 \quad (\text{A5c})$$

everywhere in space. We note that the momentum Eq. (A5a) can be equivalently expressed as

$$-\nabla q + \mu \nabla^2 \mathbf{u} + \frac{S}{V} \frac{\partial \phi}{\partial z} \mathbf{e}_z = \mathbf{0}, \quad (\text{A6})$$

where V is the particle volume. If L is a typical length scale of the system (such as the jet's wavelength), then the corresponding velocity scale is $U = SL\phi/\mu V$, obtained from matching the active and viscous term in Eq. (A6).

The idea is now that the flow should, at leading order, be independent of the exact decay of ϕ in the transition region \mathcal{T} . More explicitly, we want to be able to solve Eqs. (A5a) and (A5b) in each of \mathcal{P}^- , \mathcal{P}^+ and reconstruct the overall flow by means of suitable matching across \mathcal{T} . To derive the matching conditions, we note that, within \mathcal{T} ,

$$|\partial_i \partial_j u_k| \sim U/\delta L, \quad (\text{A7a})$$

$$|\partial_i u_j| \sim U/L, \quad (\text{A7b})$$

$$|u_i| \sim U, \quad (\text{A7c})$$

for each i, j, k . Here Eq. (A7a) comes from balancing the viscous and (large) active term of (A6), while Eq. (A7b) and (A7c) are then obtained by successively integrating Eq. (A7a) across \mathcal{T} . Intuitively, Eq. (A7a) through (A7c) imply that the transition region \mathcal{T} is characterized by rapidly changing, although bounded, velocity gradients.

We then see, from Eq. (A7b), that for each $\mathbf{x} \in \partial\mathcal{P}^-$,

$$\|\mathbf{u}|_{\mathbf{x}} - \mathbf{u}|_{\chi(\mathbf{x})}\| = \mathcal{O}(U\delta/L). \quad (\text{A8})$$

In other words, the velocity is approximately continuous across \mathcal{T} .

Secondly, we may define a *pillbox* spanning \mathcal{T} , consisting of the volume enclosed between the area patches $\mathcal{A} \in \partial\mathcal{P}^-$ and $\chi(\mathcal{A}) \in \partial\mathcal{P}^+$. We assume that \mathcal{A} and, therefore, $\chi(\mathcal{A})$ have typical size $(\delta L)^{1/2}$. Integrating the momentum equation $\partial_j \Sigma_{ij} = 0$ over such a pillbox gives

$$\begin{aligned} 0 &= \int \partial_j \Sigma_{ij} dV \\ &= \int_{\mathcal{A}} \Sigma_{ij} n_j dA + \int_{\chi(\mathcal{A})} \Sigma_{ij} n_j dA + \mathcal{O}(\mu \delta^{3/2} U/L^{1/2}) \\ &= \Sigma_{ij} n_j|_{\mathbf{x}} \cdot \|\mathcal{A}\| + \Sigma_{ij} n_j|_{\chi(\mathbf{x})} \cdot \|\chi(\mathcal{A})\| + \mathcal{O}(\mu \delta^{3/2} U/L^{1/2}) \\ &= \Sigma_{ij} n_j|_{\mathbf{x}} \cdot \|\mathcal{A}\| + \Sigma_{ij} n_j|_{\chi(\mathbf{x})} \cdot \|\mathcal{A}\| + \mathcal{O}(\mu \delta^{3/2} U/L^{1/2}). \end{aligned} \quad (\text{A9})$$

This shows that

$$\|\boldsymbol{\Sigma} \cdot \mathbf{n}|_{\mathbf{x}} - \boldsymbol{\Sigma} \cdot \mathbf{n}|_{\chi(\mathbf{x})}\| = \mathcal{O}(\mu \delta^{1/2} U/L^{3/2}). \quad (\text{A10})$$

In other words, stresses are approximately continuous across \mathcal{T} .

The leading-order flow with respect to the small parameter $(\delta/L)^{1/2}$ therefore obeys

\mathcal{P}^-	\mathcal{P}^+	$\partial\mathcal{P}^-$
$\partial_j \Sigma_{ij}^- = 0 \quad (\text{A11a})$	$\partial_j \Sigma_{ij}^+ = 0 \quad (\text{A12a})$	$\Sigma_{ij}^- n_j _{\mathbf{x}} = \Sigma_{ij}^+ n_j _{\chi(\mathbf{x})} \quad (\text{A13a})$
$\partial_i u_i^- = 0 \quad (\text{A11b})$	$\partial_i u_i^+ = 0 \quad (\text{A12b})$	$u_i^- _{\mathbf{x}} = u_i^+ _{\chi(\mathbf{x})} \quad (\text{A13b})$

The key step is now that if the flows in \mathcal{P}^+ and \mathcal{P}^- do indeed vary on the large length scale L , then we may evaluate the boundary conditions (A13a) and (A13b) at \mathbf{x} , rather than $\chi(\mathbf{x})$. Doing so yields

the correct velocity fields in \mathcal{P}^- , \mathcal{P}^+ up to $\mathcal{O}(\delta U/L)$, which can be neglected consistently with the previous approximation. Furthermore, because the velocity varies on a length scale L , the flow in the transition region \mathcal{T} is also determined with the same error. Imposing the boundary conditions at \mathbf{x} is allowed, provided we check *a posteriori* that the flows vary on the correct length scale. The simplified equations now read

\mathcal{P}^-	\mathcal{P}^+	$\partial\mathcal{P}^-$
$\partial_j \Sigma_{ij}^- = 0 \quad (\text{A14a})$	$\partial_j \Sigma_{ij}^+ = 0 \quad (\text{A15a})$	$\Sigma_{ij}^- n_j _{\mathbf{x}} = \Sigma_{ij}^+ n_j _{\mathbf{x}} \quad (\text{A16a})$
$\partial_i u_i^- = 0 \quad (\text{A14b})$	$\partial_i u_i^+ = 0 \quad (\text{A15b})$	$u_i^- _{\mathbf{x}} = u_i^+ _{\mathbf{x}} \quad (\text{A16b})$

which are the same as Eqs. (7a) through (9b) in the main text; these equations uniquely determine the leading-order flow.

We must now verify that the flow indeed varies on a length scale L . We note that, because the concentration is constant in \mathcal{P}^- , \mathcal{P}^+ , the simplified equation reduce to the Stokes equations with a stress-jump boundary condition given by

\mathcal{P}^-	\mathcal{P}^+	$\partial\mathcal{P}^-$
$\partial_j \sigma_{ij}^- = 0 \quad (\text{A17a})$	$\partial_j \sigma_{ij}^+ = 0 \quad (\text{A18a})$	$\sigma_{ij}^+ n_j _{\mathbf{x}} = \sigma_{ij}^- n_j _{\mathbf{x}} + \frac{S\phi_0}{V} p_i p_j n_j \quad (\text{A19a})$
$\partial_i u_i^- = 0 \quad (\text{A17b})$	$\partial_i u_i^+ = 0 \quad (\text{A18b})$	$u_i^- _{\mathbf{x}} = u_i^+ _{\mathbf{x}} \quad (\text{A19b})$

such equations have a unique solution varying on the length scale L , which completes our check *a posteriori*. We remark that, although Eqs. (7a) through (9b) yield the correct leading-order flow everywhere, they do not give the correct velocity gradients or stresses in \mathcal{T} , as in our approximation all quantities vary on a length scale L , but gradient in \mathcal{T} vary on a length scale δ . This is, however, inconsequential for the interfacial dynamics, Eq. (A5c), which is completely determined by the velocity field.

2. Stresslet flow superposition

An alternative, flow-focused derivation of the continuum equations may be found directly from an application of the Saintillan and Shelley formalism [8–10]. As a first step, we note that the flow created by a single dipole located at \mathbf{x}_0 and oriented along \mathbf{e}_z satisfies

$$\nabla q^d(\mathbf{x}; \mathbf{x}_0) - \mu \nabla^2 \mathbf{u}^d(\mathbf{x}; \mathbf{x}_0) = -S \mathbf{e}_z \mathbf{e}_z \cdot \nabla_0 \delta^{(3)}(\mathbf{x} - \mathbf{x}_0). \quad (\text{A20})$$

The velocity field \mathbf{u} in a dilute suspension of such dipoles with local volume fraction $\phi(\mathbf{x})$ can then be obtained by superposing the \mathbf{u}^d , q^d for each value of \mathbf{x}_0 . Therefore, the bulk flow satisfies

$$\nabla q(\mathbf{x}) - \mu \nabla^2 \mathbf{u}(\mathbf{x}) = -\frac{S}{V} \mathbf{e}_z \mathbf{e}_z \cdot \int_{\mathbb{R}^3} \phi(\mathbf{x}_0) \nabla_0 \delta^{(3)}(\mathbf{x} - \mathbf{x}_0) d^3 \mathbf{x}_0. \quad (\text{A21})$$

We want to analyze the case of a piecewise smooth concentration, i.e., a field $\phi(\mathbf{x})$ which is smooth in two disjoint open regions \mathcal{P}^- and \mathcal{P}^+ (with $\mathbb{R}^3 = \mathcal{P}^- \cup \mathcal{P}^+$) but discontinuous at the interface $\partial\mathcal{P}^- = \partial\mathcal{P}^+ =: \partial\mathcal{P}$. Splitting up the integral over each region and applying the divergence

theorem, we find (for $\mathbf{x} \notin \partial\mathcal{P}$)

$$\begin{aligned}
 \nabla q(\mathbf{x}) - \mu \nabla^2 \mathbf{u}(\mathbf{x}) &= -\frac{S}{V} \int_{\mathcal{P}^-} \phi(\mathbf{x}_0) \mathbf{e}_z \mathbf{e}_z \cdot \nabla_0 \delta^{(3)}(\mathbf{x} - \mathbf{x}_0) d^3 \mathbf{x}_0 \\
 &\quad - \frac{S}{V} \int_{\mathcal{P}^+} \phi(\mathbf{x}_0) \mathbf{e}_z \mathbf{e}_z \cdot \nabla_0 \delta^{(3)}(\mathbf{x} - \mathbf{x}_0) d^3 \mathbf{x}_0 \\
 &= \frac{S}{V} \int_{\mathbb{R}^3} \delta^{(3)}(\mathbf{x} - \mathbf{x}_0) \mathbf{e}_z \mathbf{e}_z \cdot \nabla_0 \phi(\mathbf{x}_0) d^3 \mathbf{x}_0 \\
 &\quad + \frac{S}{V} \oint_{\partial\mathcal{P}} \delta^{(3)}(\mathbf{x} - \mathbf{x}_0) [\phi]_-^+ \mathbf{e}_z (\mathbf{e}_z \cdot \mathbf{n}) dA \\
 &= \frac{S}{V} \mathbf{e}_z \mathbf{e}_z \cdot \nabla \phi(\mathbf{x}) + \frac{S}{V} \oint_{\partial\mathcal{P}} \delta^{(3)}(\mathbf{x} - \mathbf{x}_0) [\phi]_-^+ \mathbf{e}_z (\mathbf{e}_z \cdot \mathbf{n}) dA. \tag{A22}
 \end{aligned}$$

The final term in Eq. (A22) cannot be evaluated directly, since it corresponds to the integral of the three-dimensional δ function over a surface, for which the sampling property does not apply. Equation (A22) can, however, be interpreted as a forced Stokes equation, driven by a body force $S \mathbf{e}_z \mathbf{e}_z \cdot \nabla \phi(\mathbf{x})/V$ as well as a ‘‘Stokeslet membrane’’ at the interface $\partial\mathcal{P}$. The body force stems from imbalances in active stresses caused by an uneven concentration, while the boundary term captures potential force imbalances at the interface. The strength density of the Stokeslets can be read off to be $S[\phi]_-^+ \mathbf{e}_z (\mathbf{e}_z \cdot \mathbf{n})/V$. We may now solve for the total flow \mathbf{u} by superposing the flow induced by the Stokeslet membrane with the flow driven by the body force, found from the integral solution of the Stokes equations [45,46]:

$$\mathbf{u}(\mathbf{x}) = \frac{S}{V} \int_{\mathbb{R}^3} [\mathbf{J}(\mathbf{x} - \mathbf{y}) \cdot \mathbf{e}_z] [\mathbf{e}_z \cdot \nabla \phi(\mathbf{y})] d^3 \mathbf{y} + \frac{S}{V} \oint_{\partial\mathcal{P}} \mathbf{J}(\mathbf{x} - \mathbf{y}) \cdot \mathbf{e}_z (\mathbf{e}_z \cdot \mathbf{n}) [\phi]_-^+ dA. \tag{A23}$$

This is the same as the solution to the forced Stokes equation with stress jump conditions [45,46]

$$\nabla q - \mu \nabla^2 \mathbf{u} = \frac{S}{V} \mathbf{e}_z \mathbf{e}_z \cdot \nabla \phi(\mathbf{x}), \quad \mathbf{x} \notin \partial\mathcal{P} \tag{A24a}$$

$$[-q\mathbf{I} + \mu(\nabla \mathbf{u} + \nabla \mathbf{u}^T)]_-^+ \cdot \mathbf{n} = -\frac{S}{V} [\phi]_-^+ \mathbf{e}_z (\mathbf{e}_z \cdot \mathbf{n}), \quad \mathbf{x} \in \partial\mathcal{P}, \tag{A24b}$$

which are precisely the forced Stokes equations that we solve in the main text. When the bulk concentration is piecewise constant, the body force in Eq. (A22) disappears, as all stresslets cancel in the bulk. The only remaining term is the Stokeslet membrane, which arises because swimmers on one side of the interface push or pull harder than on the other.

APPENDIX B: GROWTH RATE OF A THREE-DIMENSIONAL JET

In this section, we delve into the calculation of the $\mathcal{O}(\varepsilon)$ flow determining the stability of a three-dimensional jet [Eqs. (20a) through (22c)]. We denote the flows outside and inside the jet as $\mathbf{u}_1^\pm = u_1^\pm \mathbf{e}_r + v_1^\pm \mathbf{e}_\theta + w_1^\pm \mathbf{e}_z$ (respectively), and the corresponding pressures as q_1^\pm . In order to solve for the flow, we take the Fourier transform of Eqs. (20a)–(22c) in the z and θ directions, thereby assuming

$$u_1^\pm = U_1^\pm(r) e^{ikz + in\theta + st}, \tag{B1a}$$

$$v_1^\pm = -iV_1^\pm(r) e^{ikz + in\theta + st}, \tag{B1b}$$

$$w_1^\pm = W_1^\pm(r) e^{ikz + in\theta + st}, \tag{B1c}$$

$$q_1^\pm = Q_1^\pm(r) e^{ikz + in\theta + st}. \tag{B1d}$$

The calculation then proceeds as follows: we first determine the pressures q_1^\pm , and use these to derive a system of coupled ODEs for the velocity fields, which are determined up to multiplicative

constants. Imposing continuity of stress, Eq. (22a), and velocity, Eq. (22b), at the jet boundary, as well as the kinematic boundary condition, Eq. (22c), results in a homogeneous linear system for the flow parameters. Such a system only admits nonzero solutions for the flow when the growth rate s takes a particular value. This allows us to fully determine the growth rate as a function of the axial and azimuthal wave numbers k and n .

In all that follows, we make use of the classical Bessel function identities [41,42]

$$K'_n - \frac{n}{z}K_n = -K_{n+1}, \quad (\text{B2a})$$

$$K'_n + \frac{n}{z}K_n = -K_{n-1}, \quad (\text{B2b})$$

$$K_{n-2} + \frac{2}{z}(n-1)K_{n-1} = K_n, \quad (\text{B2c})$$

$$I'_n - \frac{n}{z}I_n = I_{n+1}, \quad (\text{B3a})$$

$$I'_n + \frac{n}{z}I_n = I_{n-1}, \quad (\text{B3b})$$

$$I_{n-2} - \frac{2}{z}(n-1)I_{n-1} = I_n. \quad (\text{B3c})$$

In order to include the axisymmetric case $n = 0$ in the analysis, we define $I_{-n}(z) := I_n(z)$, $K_{-n}(z) := K_n(z)$ for $n > 0$, which still obey the above properties.

Because the pressures must satisfy Laplace's equation $\nabla^2 q_1^\pm = 0$, we immediately conclude that

$$r^2 \frac{d^2 Q_1^\pm}{dr^2} + r \frac{dQ_1^\pm}{dr} - (n^2 + k^2 r^2) Q_1^\pm = 0 \quad \Rightarrow \quad \begin{aligned} Q_1^+ &= A\mu K_n(kr), \\ Q_1^- &= D\mu I_n(kr), \end{aligned} \quad (\text{B4a})$$

$$(\text{B4b})$$

where we imposed the outer pressure field, Eq. (B4a), to decay at $r \rightarrow \infty$ and the inner pressure field, Eq. (B4b), to be regular at $r = 0$.

1. Outer velocity field

We may now use Eqs. (B4a) and (B4b) to solve for the velocities. We start by determining the outer velocity fields, which are found by taking the r and θ component of the Stokes equation, Eq. (21a), with the pressure field from Eq. (B4a):

$$\frac{d^2 U_1^+}{dr^2} + \frac{1}{r} \frac{dU_1^+}{dr} - \left(k^2 + \frac{n^2 + 1}{r^2} \right) U_1^+ - \frac{2n}{r^2} V_1^+ = AkK'_n(kr), \quad (\text{B5a})$$

$$\frac{d^2 V_1^+}{dr^2} + \frac{1}{r} \frac{dV_1^+}{dr} - \left(k^2 + \frac{n^2 + 1}{r^2} \right) V_1^+ - \frac{2n}{r^2} U_1^+ = -\frac{An}{r} K_n(kr). \quad (\text{B5b})$$

Adding and subtracting Eqs. (B5a), (B5b), and using properties (B2a) through (B2c), we obtain the following uncoupled equations for $U_1^+ + V_1^+$ and $U_1^+ - V_1^+$:

$$\left[\frac{d^2}{dr^2} + \frac{1}{r} \frac{d}{dr} - \frac{(n+1)^2}{r^2} - k^2 \right] (U_1^+ + V_1^+) = AkK'_n(kr) - \frac{An}{r} K_n(kr) = -AkK_{n+1}(kr), \quad (\text{B6a})$$

$$\left[\frac{d^2}{dr^2} + \frac{1}{r} \frac{d}{dr} - \frac{(n-1)^2}{r^2} - k^2 \right] (U_1^+ - V_1^+) = AkK'_n(kr) + \frac{An}{r} K_n(kr) = -AkK_{n-1}(kr). \quad (\text{B6b})$$

We may solve Eqs. (B6a) and (B6b) exactly by exploiting properties (B2a) through (B2c), giving

$$U_1^+ + V_1^+ = \frac{1}{2}ArK_n + BK_{n+1}, \quad U_1^+ = \frac{1}{2}[ArK_n + BK_{n+1} + CK_{n-1}], \quad (\text{B8a})$$

$$U_1^+ - V_1^+ = \frac{1}{2}ArK_n + CK_{n-1}, \quad V_1^+ = \frac{1}{2}[BK_{n+1} - CK_{n-1}]. \quad (\text{B8b})$$

The axial flow is found from the incompressibility condition, Eq. (21b), to be

$$W_1^+ = \frac{i}{k} \left(\frac{\partial U_1^+}{\partial r} + \frac{U_1^+}{r} + n \frac{V_1^+}{r} \right) = \frac{i}{2k} \{[(2-n)A - Bk - Ck]K_n - AkrK_{n-1}\}. \quad (\text{B9})$$

2. Inner velocity field

An analogous procedure allows us to determine the inner velocity fields. The r and θ components of the Stokes equation, Eq. (20a), with pressure field from Eq. (B4b), are

$$\frac{d^2 U_1^-}{dr^2} + \frac{1}{r} \frac{dU_1^-}{dr} - \left(k^2 + \frac{n^2 + 1}{r^2} \right) U_1^- - \frac{2n}{r^2} V_1^+ = DkI'_n(kr), \quad (\text{B10a})$$

$$\frac{d^2 V_1^-}{dr^2} + \frac{1}{r} \frac{dV_1^-}{dr} - \left(k^2 + \frac{n^2 + 1}{r^2} \right) V_1^- - \frac{2n}{r^2} U_1^- = -\frac{Dn}{r} I_n(kr). \quad (\text{B10b})$$

We may decouple Eqs. (B10a) and (B10b) by adding and subtracting them, and using properties (B3a) through (B3c):

$$\left[\frac{d^2}{dr^2} + \frac{1}{r} \frac{d}{dr} - \frac{(n+1)^2}{r^2} - k^2 \right] (U_1^- + V_1^-) = DkI'_n(kr) - \frac{Dn}{r} I_n(kr) = DkI_{n+1}(kr), \quad (\text{B11a})$$

$$\left[\frac{d^2}{dr^2} + \frac{1}{r} \frac{d}{dr} - \frac{(n-1)^2}{r^2} - k^2 \right] (U_1^- - V_1^-) = DkI'_n(kr) + \frac{Dn}{r} I_n(kr) = DkI_{n-1}(kr). \quad (\text{B11b})$$

Once again, Eqs. (B11a) and (B11b) may be solved exactly by exploiting properties (B3a) through (B3c), giving

$$U_1^- + V_1^- = \frac{1}{2} Dr I_n + F I_{n+1}, \quad \Rightarrow \quad U_1^- = \frac{1}{2} [Dr I_n + F I_{n+1} + G I_{n-1}], \quad (\text{B13a})$$

$$U_1^- - V_1^- = \frac{1}{2} Dr I_n + G I_{n-1}, \quad \Rightarrow \quad V_1^- = \frac{1}{2} [F I_{n+1} - G I_{n-1}]. \quad (\text{B13b})$$

As before, the inner axial velocity follows from the incompressibility condition, Eq. (20b), as

$$W_1^- = \frac{i}{k} \left(\frac{\partial U_1^-}{\partial r} + \frac{U_1^-}{r} + n \frac{V_1^-}{r} \right) = \frac{i}{2k} \{[(2-n)D + Fk + Gk]I_n(kr) + DkrI_{n-1}(kr)\}. \quad (\text{B14})$$

3. Determining the growth rate

Having determined the velocity fields, Eqs. (B8a), (B8b), (B9), (B13a), (B13b), and (B14), and the pressure fields, Eqs (B4a) and (B4b), we next impose continuity of stress at the jet boundary, Eq. (22a), and of velocity, Eq. (22b), as well as the kinematic boundary condition, Eq. (22c). Doing so yields a homogeneous linear system (too cumbersome to write down explicitly) for the previously identified flow parameters A, B, C, D, F, G , which must have vanishing determinant in order to admit a nonzero solution for the flow. Imposing the determinant of the linear system to vanish sets the the growth rate to be exactly

$$\text{Re}(s) = \frac{S\phi_0}{2\mu V} \frac{I_n(\xi)[K_n(\xi)(2n^2 + \xi^2) - n\xi K_{n+1}(\xi)] - I_{n+1}(\xi)[\xi^2 K_{n+1}(\xi) - n\xi K_n(\xi)]}{\xi I_n(\xi)K_{n+1}(\xi) + \xi K_n(\xi)I_{n+1}(\xi)}, \quad (\text{B15})$$

which is Eq. (23) in the main text.

APPENDIX C: ASYMPTOTIC BEHAVIOR OF THE GROWTH RATE OF A THREE-DIMENSIONAL JET

In this Appendix, we aim to thoroughly investigate the stability of a three-dimensional jet given the explicit expression in Eq. (B15) for the growth rate of a given mode (ξ, n) . Specifically, we aim to determine:

(1) A classification of the modes (ξ, n) that lead to a growing or a decaying boundary perturbation for pushers and pullers. This is of interest, as it sheds light on the physical mechanism behind the observed instability.

(2) The fastest-growing mode depending on whether the jet is made of pushers or pullers. Mathematically, this corresponds to the pair (ξ, n) with the largest $\text{Re}(s)$ [Eq. (B15)] for $S < 0$ and $S > 0$. This is significant, as the fastest-growing mode is the one observed in experiments and numerical simulations.

1. Growing and decaying modes for pushers and pullers

Based on direct numerical evaluation (Fig. 3) of the growth rate from Eq. (B15), it appears that, for $S > 0$ (pullers), a given mode (ξ, n) results in a decaying perturbation for $\xi \lesssim qn$, and a growing perturbation for $\xi \gtrsim qn$, for some constant q . Conversely, for $S < 0$ (pushers), a given mode (ξ, n) results in a decaying perturbation for $\xi \gtrsim qn$, and a growing perturbation for $\xi \lesssim qn$. Inspired by these preliminary results, we may carry out a more precise analysis to identify the exact value of the constant q . To this end, we expand for $n \rightarrow \infty$

$$I_n(qn) \sim \frac{\sqrt{2}q^n e^{n(q^2+1)^{1/2}}}{\sqrt{\pi}(q^2+1)^{13/4}[1+(q^2+1)^{1/2}]^n} \times \left[\frac{(q^2+1)^3}{2n^{1/2}} + \frac{3(q^2+1)^{5/2} - 5(q^2+1)^{3/2}}{48n^{3/2}} + \frac{4 - 300q^2 + 81q^4}{2304n^{5/2}} + \mathcal{O}(n^{-7/2}) \right], \quad (\text{C1a})$$

$$K_n(qn) \sim \frac{\sqrt{2\pi}e^{-n(1+q^2)^{1/2}}[1+(1+q^2)^{1/2}]^n}{q^n(q^2+1)^{13/4}} \times \left[\frac{(q^2+1)^3}{2n^{1/2}} + \frac{5(q^2+1)^{3/2} - 3(q^2+1)^{5/2}}{48n^{3/2}} + \frac{4 - 300q^2 + 81q^4}{2304n^{5/2}} + \mathcal{O}(n^{-7/2}) \right]. \quad (\text{C1b})$$

Similar, although more cumbersome (and hence omitted) asymptotic expressions for $I_{n+1}(nq)$, $K_{n+1}(nq)$ may be obtained by substituting $q \rightarrow nq/(n+1)$ in the expansions of $I_{n+1}[(n+1)q]$, $K_{n+1}[(n+1)q]$ [evaluated via Eqs. (C1a) and (C1b)], and re-expanding. Such asymptotic expressions allow us to evaluate the numerator of Eq. (B15), with $\xi = qn$, as

$$\begin{aligned} \frac{2\mu V}{S\phi_0}(I_n K_{n+1} + K_n I_{n+1})qn \text{Re}(s) &= I_n[K_n(2n^2 + q^2 n^2) - qn^2 K_{n+1}] - I_{n+1}[q^2 n^2 K_{n+1} - qn^2 K_n] \\ &\sim \frac{q^2(q^2 - 2)}{4n(q^2 + 1)^{5/2}} + \mathcal{O}(n^{-2}), \end{aligned} \quad (\text{C2})$$

(all Bessel functions implicitly have argument qn) showing that, at leading order, $q = 2^{1/2}$.

2. Fastest-growing modes for pushers and pullers

Turning now our attention to the fastest-growing modes, direct numerical evaluation (Fig. 3) of the growth rate, Eq. (B15), suggests that the fastest-growing mode (ξ, n) for $S > 0$ (pullers) has $n = 0$, while the fastest-growing mode for $S < 0$ (pushers) has $n = 1$. This observation is in agreement with experiments, as $n = 0$ corresponds to a pearling mode, while $n = 1$ corresponds to a helical mode.

In order to validate these numerical findings, we evaluate the largest possible value of $\text{Re}(s)$ as a function of n (depending on whether $S > 0$ or $S < 0$) and show that, at least asymptotically, these

values decay monotonically for large n . Mathematically, this means showing that the function

$$\sigma(n) := \max_{\xi} \operatorname{Re}(s)(\xi, n) \quad (\text{C3})$$

decays monotonically as $n \rightarrow \infty$. Together with the numerical results in Fig. 3, such a behavior indicates that the absolute maximum value of $\operatorname{Re}(s)$ is attained for small values of n , specifically $n = 0$ for pullers and $n = 1$ for pushers.

For each $n \geq 1$, we numerically find two values $\xi_1^{(n)}, \xi_2^{(n)}$ such that $d\operatorname{Re}(s)/d\xi = 0$ at $\xi = \xi_{1,2}^{(n)}$, with $\xi_1^{(n)} \lesssim qn \lesssim \xi_2^{(n)}$. Such values appear to grow linearly with n , i.e., $\xi_{1,2}^{(n)} \sim q_{1,2}n$. Expanding the Bessel functions up to and including $\mathcal{O}(n^{-7/2})$ in Eqs. (C1a) and (C1b), the numerator of $d\operatorname{Re}(s)/d\xi$ is asymptotic to

$$\begin{aligned} \frac{2\mu V}{S\phi_0} (I_n K_{n+1} + K_n I_{n+1}) q_i^2 n^2 \operatorname{Re}'[s] &= 2n^3 (q_i + q_i^3) (K_n I_{n+1} - I_n K_{n+1}) + 2q_i^2 n^2 (2q_i n + 2n + 1) I_n K_n \\ &\sim -\frac{q_i^2 (q_i^4 - 10q_i^2 + 4)}{4n(q_i^2 + 1)^{7/2}} + \mathcal{O}(n^{-2}), \end{aligned} \quad (\text{C4})$$

where the Bessel functions have argument $q_i n$. The leading-order term vanishes for $q_1 = (5 - 21^{1/2})^{1/2} \sim 0.65$ and $q_2 = (5 + 21^{1/2})^{1/2} \sim 3.10$. This means that $\xi_1^{(n)} \sim 0.65n$, $\xi_2^{(n)} \sim 3.10n$. The corresponding values of $\sigma(n)$, evaluated from (C1a) and (C1b), and the expansions for $I_{n+1}[(n+1)q_i]$, $K_{n+1}[(n+1)q_i]$, are

$$\sigma(n) \sim \begin{cases} 0.02 \times \frac{S\phi_0}{\mu V n} & S > 0, \\ -0.03 \times \frac{S\phi_0}{\mu V n} & S < 0. \end{cases} \quad (\text{C5})$$

Therefore, $\sigma(n)$ decays monotonically for n large. Direct numerical evaluation of the first few values of $\sigma(n)$ in Fig. 3 then indicates that the most unstable modes are $n = 0$ for pullers and $n = 1$ for pushers.

APPENDIX D: GROWTH RATE OF A TWO-DIMENSIONAL SHEET

In this Appendix, we delve into the linear stability analysis of a variant of the three-dimensional setup considered in Appendix B. We consider the stability of a 2D sheet of swimmers (Sec. IV), initially defined by $-a \leq x \leq a$, $-\infty < y, z < \infty$ in Cartesian coordinates. We perturb the sheet boundary so that, for $t > 0$, the swimmers are located in $X^-(z, t) \leq x \leq X^+(z, t)$. We consider two forms of the perturbation:

- (1) Sinuous/in phase: $X^+ = a(1 + \varepsilon e^{st+ikz})$, $X^- = a(-1 + \varepsilon e^{st+ikz})$.
- (2) Varicose/antiphase: $X^+ = a(1 + \varepsilon e^{st+ikz})$, $X^- = a(-1 - \varepsilon e^{st+ikz})$.

In each case, we seek to determine the dispersion relation $s = s(k)$, and hence establish whether it is pushers or pullers that destabilize the sheet. For simplicity, we only show the calculation for the sinuous perturbation, which we expect to be unstable for pushers by analogy with the three-dimensional case.

By the symmetry of the setup, the x component of the velocity must be even in x , while the z component of the velocity must be odd in x . Therefore, we only need solve for the flows in the regions $X^- < x < X^+$ (denoted “−”) and $x > X^+$ (denoted “+”). Like in the three-dimensional case, we expand the velocities, pressures, and stresses in the small parameter ε :

$$\mathbf{u}^\pm = \mathbf{u}_0^\pm + \varepsilon \mathbf{u}_1^\pm + \mathcal{O}(\varepsilon^2), \quad (\text{D1a})$$

$$q^\pm = q_0^\pm + \varepsilon q_1^\pm + \mathcal{O}(\varepsilon^2), \quad (\text{D1b})$$

$$\boldsymbol{\Sigma}^\pm = \boldsymbol{\Sigma}_0^\pm + \varepsilon \boldsymbol{\Sigma}_1^\pm + \mathcal{O}(\varepsilon^2), \quad (\text{D1c})$$

and solve order by order. The base state, like in the three-dimensional case [Eq. (17)], corresponds to zero net flow, or

$$\mathbf{u}_0^\pm = \mathbf{0}, \quad q_0^\pm = 0, \quad \Sigma_0^+ = \mathbf{0}, \quad \Sigma_0^- = \frac{S\phi_0}{V} \mathbf{e}_z \mathbf{e}_z. \quad (\text{D2})$$

We now expand the flow equations (14a) through (16c) to first order, obtaining

$0 \leq x \leq a$	$a < x < \infty$	$x = a$
$\mu \nabla^2 \mathbf{u}_1^- = \nabla q_1^- \quad (\text{D3a})$	$\mu \nabla^2 \mathbf{u}_1^+ = \nabla q_1^+ \quad (\text{D4a})$	$(\Sigma_1^+ - \Sigma_1^-) \cdot \mathbf{e}_x = -\frac{S\phi_0}{V} \eta_z \mathbf{e}_z \quad (\text{D5a})$
$\nabla \cdot \mathbf{u}_1^- = 0 \quad (\text{D3b})$	$\nabla \cdot \mathbf{u}_1^+ = 0 \quad (\text{D4b})$	$\mathbf{u}_1^+ = \mathbf{u}_1^- \quad (\text{D5b})$
	$\lim_{x \rightarrow \infty} \mathbf{u}_1^+ = \mathbf{0} \quad (\text{D4c})$	$\frac{\partial \eta}{\partial t} + U_s \frac{\partial \eta}{\partial z} = \mathbf{u}_1^\pm \cdot \mathbf{e}_x \quad (\text{D5c})$

At this order, we take the Fourier transform of the velocity and pressure fields in the z direction, thereby assuming

$$u_1^\pm = U_1^\pm(x) e^{ikz+st}, \quad (\text{D6a})$$

$$v_1^\pm = V_1^\pm(x) e^{ikz+st}, \quad (\text{D6b})$$

$$q_1^\pm = Q_1^\pm(x) e^{ikz+st}. \quad (\text{D6c})$$

We now solve for the flow in a way analogous to Appendix B. Because the pressure is harmonic, we have

$$\frac{d^2 Q_1^\pm}{dx^2} - k^2 Q_1^\pm = 0 \quad \Rightarrow \quad \begin{aligned} Q_1^+ &= 2i\mu B k e^{-kx}, \\ Q_1^- &= 2i\mu k D (e^{-kx} - e^{kx}). \end{aligned} \quad (\text{D7a})$$

$$Q_1^- = 2i\mu k D (e^{-kx} - e^{kx}). \quad (\text{D7b})$$

We may now determine the velocity fields.

1. Outer velocity field

We start by determining the outer velocity fields. The x and z components of the Stokes equation, with pressure field (D7a), can be readily solved to give

$$\frac{d^2 U_1^+}{dx^2} - k^2 U_1^+ = -2iBk^2 e^{-kx}, \quad U_1^+ = i(A + Bkx) e^{-kx}, \quad (\text{D8a})$$

$$\frac{d^2 V_1^+}{dx^2} - k^2 V_1^+ = -2Bk^2 e^{-kx}, \quad V_1^+ = (A - B + Bkx) e^{-kx}. \quad (\text{D8b})$$

2. Inner velocity field

For the inner velocity field, the x and z components of the Stokes equation, with pressure field (D7b), can likewise be solved to obtain

$$\frac{d^2 U_1^-}{dx^2} - k^2 U_1^- = -2ik^2 D (e^{-kx} + e^{kx}), \quad U_1^- = i[(C + Dkx) e^{-kx} + (C - Dkx) e^{kx}], \quad (\text{D9a})$$

$$\frac{d^2 V_1^-}{dx^2} - k^2 V_1^- = -2k^2 D (e^{-kx} - e^{kx}), \quad V_1^- = (C - D + Dkx) e^{-kx} - (C - D - Dkx) e^{kx}. \quad (\text{D9b})$$

3. Determining the growth rate

As in Appendix B, having determined the full flow, Eqs. (D8a), (D8b), (D9a), and (D9b), and pressure fields, Eqs. (D7a) and (D7b), we impose continuity of stress, Eq. (D5a), and velocity,

Eq. (D5b), at the jet boundary, as well as the kinematic boundary condition, Eq. (D5c). Doing so yields a homogeneous linear system for the previously identified flow parameters A, B, C, D , which must have vanishing determinant in order to admit a nonzero solution for the flow. Imposing the determinant of the linear system to vanish leads to the following expression for the growth rate:

$$\text{Re}(s) = -\frac{S\phi_0}{2\mu V}\xi e^{-2\xi}, \quad (\text{D10})$$

where $\xi = ak$. The sheet is therefore unstable for pushers, for which $S < 0$.

The varicose perturbation case $X^+ = a(1 + \varepsilon e^{st+ikz})$, $X^- = a(-1 - \varepsilon e^{ikz+st})$ can be handled similarly, this time making the x component of velocity odd in x and the z component of velocity even in x . A similar calculation as above then yields

$$\text{Re}(s) = \frac{S\phi_0}{2\mu V}\xi e^{-2\xi} \quad (\text{D11})$$

for the varicose perturbation. The sheet is therefore unstable for pullers, for which $S > 0$.

APPENDIX E: EVOLUTION OF PULLER CLUSTERS

In this Appendix, we derive exact solutions for the long-term evolution of 3D and 2D clusters of pullers. We show that such solutions exist under the assumption that the cluster is initially a sphere (in 3D) or a circle (in 2D). We then specialize our solutions to the limit of a thin cluster. This is the most experimentally significant regime, as the initial shape of the cluster is forgotten and the dynamics is self-similar, with the rate of spreading set purely by the active stresses and the initial cluster volume (area).

1. Analytical solution for the spreading of a spherical cluster

Assuming that the initial cluster is spherical with constant volume fraction ϕ_0 and that the swimming direction is fixed to be $\mathbf{p} \equiv \mathbf{e}_z$, the subsequent evolution in the limit of a sharp concentration drop outside the cluster is governed by Eq. (14a) through (16c). These equations may be solved exactly by noting that, at any point during the shape evolution, the active stress $S\phi_0(\mathbf{e}_z \cdot \mathbf{n})\mathbf{e}_z/V$ on the boundary of the cluster is of the same form (up to an isotropic part) as the stress exerted by an axisymmetric straining flow, $\mathbf{u} = \mathbf{E} \cdot \mathbf{x} = E(r\mathbf{e}_r - 2z\mathbf{e}_z)$, inside the cluster. Assuming that this is indeed the internal flow at each point in time, we expect the initially spherical cluster to progressively deform into an oblate ellipsoid with semimajor axis $R(t)$.

In order to compute the shape evolution, we need to determine the time-dependent straining rate $E = E(t)$ and internal pressure $p_0 = p_0(t)$ by imposing that the internal viscous and active stresses balance the external viscous stresses at the cluster boundary. To this end, we note that the external flow $\bar{\mathbf{u}}$ is driven by the boundary condition $\mathbf{u} = \bar{\mathbf{u}}$ on the boundary of the cluster. The external flow therefore corresponds to the opposite of the perturbation flow induced by a (fictitious) rigid ellipsoid in strain flow. Therefore, the internal active stresses $-p_0\mathbf{n} + S\phi_0(\mathbf{e}_z \cdot \mathbf{n})\mathbf{e}_z/V$ must be equal to the force exerted by a rigid ellipsoid in strain flow, given by

$$\bar{\boldsymbol{\sigma}} \cdot \mathbf{n} = -\mu E \left[\frac{1}{3F(\chi)} + \frac{G(\chi)}{3F(\chi)} \right] \mathbf{n} + \frac{\mu E}{F(\chi)} (\mathbf{e}_z \cdot \mathbf{n}) \mathbf{e}_z, \quad (\text{E1})$$

for known functions F, G of the ellipsoid's aspect ratio χ ($0 < \chi < 1$) [47]. Stress continuity allows us to determine the constant internal pressure p_0 and the strain rate, given by

$$E = \frac{S\phi_0}{\mu V} F(\chi). \quad (\text{E2})$$

We thus obtain that the semimajor axis satisfies the evolution equation

$$\frac{dR}{dt} = \frac{S\phi_0}{\mu V} R F(\chi), \quad (\text{E3a})$$

$$F(\chi) = \frac{1}{4(1-\chi^2)^2} \left[-3\chi^2 + \frac{\chi(1+2\chi^2)}{(1-\chi^2)^{1/2}} \cos^{-1} \chi \right], \quad (\text{E3b})$$

$$R(0) = R_0. \quad (\text{E3c})$$

Since the cluster is deformed by incompressible flow, the volume has to be conserved. Expressing therefore $\chi = R_0^3/R^3$ (R_0 being the initial radius), and choosing units in which $R_0 = 1$, Eq. (E3) may be recast into Eqs. (30a) and (30b) from the main text.

Thin limit of a stretching 3D cluster

As the cluster becomes more and more elongated, the initial shape is forgotten and a self-similar solution is reached, dependent only on the initial cluster volume. The stresses on the cluster boundary may be found in this limit by noting that the unit normal and radially tangent vectors \mathbf{n} and \mathbf{t} on the top surface $z = \chi(R^2 - r^2)^{1/2}$ take the form

$$\mathbf{n} = \frac{\chi r}{(R^2 - r^2)^{1/2}} \mathbf{e}_r + \mathbf{e}_z + \mathcal{O}(\chi^2), \quad (\text{E4})$$

$$\mathbf{t} = \mathbf{e}_r - \frac{\chi r}{(R^2 - r^2)^{1/2}} \mathbf{e}_z + \mathcal{O}(\chi^2). \quad (\text{E5})$$

Considering the normal and tangential components of Eq. (E1), by virtue of the asymptotic behaviors $F \sim \pi\chi/8 + \mathcal{O}(\chi^2)$, $G \sim 2 + \mathcal{O}(\chi)$ for $\chi \rightarrow 0$ [47], we find

$$\mathbf{n} \cdot \bar{\boldsymbol{\sigma}} \cdot \mathbf{n} \sim \text{const}, \quad (\text{E6})$$

$$\mathbf{t} \cdot \bar{\boldsymbol{\sigma}} \cdot \mathbf{n} \sim -\frac{8}{\pi} \frac{\mu E r}{(R^2 - r^2)^{1/2}}. \quad (\text{E7})$$

These expressions correspond to the normal and tangential tractions exerted by a thin rigid disk in axisymmetric straining flow. To compute the long-term evolution of the cluster, we take $\chi \rightarrow 0$ in Eqs. (E3a) and (E3b), obtaining

$$\frac{dR}{dt} = \frac{S\phi_0}{\mu V} \frac{3V_0}{32R^2}. \quad (\text{E8})$$

Integrating Eq. (E8), and substituting the result into Eq. (E2), we find

$$R \sim \left(\frac{9}{32} \frac{S\phi_0 V_0}{\mu V} \right)^{1/3} t^{1/3}, \quad (\text{E9a})$$

$$E \sim \frac{1}{3} t^{-1}. \quad (\text{E9b})$$

Note that the results in Eqs. (E9a) and (E9b) are valid for $R \gg V_0^{1/3}$, corresponding to the limit

$$t \gg \frac{\mu V}{S\phi_0}, \quad (\text{E10})$$

i.e., long after the initial instability.

2. Analytical solution for spreading of a 2D circular cluster

A similar calculation may be carried out for a 2D cluster. Focusing on the deformation of a single 2D slice, similar arguments as in the 3D case show that the flow inside the cluster is a pure strain, of the form $\mathbf{u} = \mathbf{E} \cdot \mathbf{x} = E(x, -z)$. We therefore expect the slice to deform into an ellipse of semimajor axis $R(t)$. In order to determine the time-dependent rate of strain $E(t)$ and internal pressure $p_0(t)$,

we impose stress continuity at the boundary of the ellipse. Much like in 3D, the external flow is the negative of the perturbation flow experienced by a (fictitious) rigid ellipse in strain flow. The corresponding external stress exerted by the ellipse is [54]

$$\bar{\sigma} \cdot \mathbf{n} = -\frac{\mu(1+\chi)^2}{\chi} \mathbf{E} \cdot \mathbf{n}, \quad (\text{E11})$$

where $0 < \chi < 1$ is the aspect ratio. Imposing that this stress balances the internal stresses $-p_0 \mathbf{n} + S\phi_0(\mathbf{e}_z \cdot \mathbf{n})\mathbf{e}_z/V$ determines the straining rate to be

$$E = \frac{S\phi_0}{2\mu V} \frac{\chi}{(1+\chi)^2}. \quad (\text{E12})$$

Expressing $\chi = R_0^2/R^2$ from area conservation (since the cluster is deformed by incompressible flow), we obtain the evolution equation in the 2D case:

$$\frac{dR}{dt} = \frac{S\phi_0}{\mu V} \frac{\chi R}{2(1+\chi)^2}, \quad (\text{E13})$$

$$R(0) = R_0. \quad (\text{E14})$$

After choosing units in which $R_0 = 1$, this may be recast into Eqs. (31a) and (31b) in the main text.

Thin limit of a stretching 2D cluster

As the cluster becomes more and more elongated, the initial shape is forgotten and a self-similar solution is reached, dependent only on the initial cluster volume. The stresses on the cluster boundary may be found in this limit by noting that the unit normal and tangent vectors \mathbf{n} and \mathbf{t} on the top surface $z = \chi(R^2 - x^2)^{1/2}$ take the form

$$\mathbf{n} = \frac{\chi x}{(R^2 - x^2)^{1/2}} \mathbf{e}_x + \mathbf{e}_z + \mathcal{O}(\chi^2), \quad (\text{E15})$$

$$\mathbf{t} = \mathbf{e}_x - \frac{\chi x}{(R^2 - x^2)^{1/2}} \mathbf{e}_z + \mathcal{O}(\chi^2). \quad (\text{E16})$$

Considering the normal and tangential components of Eq. (E11), we obtain

$$\mathbf{n} \cdot \bar{\sigma} \cdot \mathbf{n} \sim \text{const}, \quad (\text{E17})$$

$$\mathbf{t} \cdot \bar{\sigma} \cdot \mathbf{n} \sim \frac{2\mu E x}{(R^2 - x^2)^{1/2}}. \quad (\text{E18})$$

These expressions correspond to the normal and tangential tractions exerted by a rigid rod in 2D strain flow. To compute the long-term evolution of the cluster, we take $\chi \rightarrow 0$ in Eq. (E13), obtaining

$$\frac{dR}{dt} = \frac{S\phi_0}{\mu V} \frac{A_0}{2\pi R}. \quad (\text{E19})$$

Integrating Eq. (E19), and substituting the result into Eq. (E12), we find

$$R \sim \left(\frac{S\phi_0 A_0}{\pi \mu V} \right)^{1/2} t^{1/2}, \quad (\text{E20})$$

$$E \sim \frac{1}{2} t^{-1}. \quad (\text{E21})$$

Equations (E20) and (E21) are again valid in the limit

$$t \gg \frac{\mu V}{S\phi_0}, \quad (\text{E22})$$

i.e., long after the initial instability.

3. Interactions between clusters

In our previous analysis (Appendixes E 1 and E 2), we neglected interactions between clusters. We may now use the previously determined external flows to recover leading-order cluster-cluster interactions, in the limit where clusters only interact in the far field (i.e., the typical cluster size is much smaller than the typical separation length). In this case, because the leading-order external flow is the same as the (negative) perturbation flow of a rigid oblate ellipsoid (3D) or an ellipse (2D) in a strain flow, clusters interact primarily as stresslets. We now determine the strength of the stresslets in each of the 3D and the 2D cases.

a. Flow outside a 3D cluster

The flow outside a 3D cluster is, at leading order, the same as the negative of the perturbation flow created by an equivalent rigid oblate ellipsoid in the strain flow $\mathbf{u} = \mathbf{E} \cdot \mathbf{x}$, where \mathbf{E} is the same as for the internal strain flow. Such a perturbation flow may be approximated by its leading-order, corresponding to a stresslet flow [47]

$$\mathbf{u}^p = -\frac{3(\mathbf{x} \cdot \mathbf{S} \cdot \mathbf{x})\mathbf{x}}{8\pi\mu r^5} + \mathcal{O}(r^{-3}) \quad (\text{E23})$$

where, by Eq. (2) and the divergence theorem,

$$\begin{aligned} S_{ij} &= \frac{S\phi_0}{V} \int_{\partial B} \frac{1}{2} [x_j(\mathbf{e}_z)_i(\mathbf{e}_z)_k b_k + x_i(\mathbf{e}_z)_j(\mathbf{e}_z)_k b_k] - \frac{1}{3} [x_k(\mathbf{e}_z)_k(\mathbf{e}_z)_l b_l] \delta_{ij} dA \\ &= \frac{S\phi_0 V_0}{V} \left[(\mathbf{e}_z)_i(\mathbf{e}_z)_j - \frac{1}{3} \delta_{ij} \right]. \end{aligned} \quad (\text{E24})$$

Recognizing $\phi_0 V_0/V$ as the total number of swimmers, S_{ij} is thus simply the sum of all internal stresslets.

b. Flow outside a 2D cluster

Likewise, for the 2D cluster, the external flow is at leading order [44]

$$\mathbf{u} = -\frac{(\mathbf{x}^\perp \cdot \mathbf{S} \cdot \mathbf{x}^\perp)\mathbf{x}^\perp}{2\pi\mu\rho^4} + \mathcal{O}(\rho^{-2}), \quad (\text{E25})$$

where \mathbf{x}^\perp is the component of \mathbf{x} perpendicular to the axis of the cluster, $\rho = \|\mathbf{x}^\perp\|$, and the stresslet (per unit extent in the y direction) is

$$\begin{aligned} S_{ij} &= \frac{S\phi_0}{V} \int_{\partial B} \frac{1}{2} [x_j(\mathbf{e}_z)_i(\mathbf{e}_z)_k b_k + x_i(\mathbf{e}_z)_j(\mathbf{e}_z)_k b_k] - \frac{1}{2} [x_k(\mathbf{e}_z)_k(\mathbf{e}_z)_l b_l] \delta_{ij}^{(2)} ds \\ &= \frac{S\phi_0 A_0}{V} \left[(\mathbf{e}_z)_i(\mathbf{e}_z)_j - \frac{1}{2} \delta_{ij}^{(2)} \right], \end{aligned} \quad (\text{E26})$$

where $\delta_{ij}^{(2)}$ is the identity tensor in \mathbb{R}^2 and s is arclength. Once again, $\phi_0 A_0/V$ is the number of swimmers per unit length, so that S_{ij} is the sum of the internal stresslets. In light of the far-field flows in both 3D and 2D, we expect puller clusters to interact like a line of stresslets (see Sec. VC).

4. Analytical solution for a tilted puller cluster

In this section, we derive the analytical solution for the flow inside a tilted puller cluster, as summarized in Sec. VD of the main text. We are going to assume (and later verify) that tilted clusters deform exactly as ellipses of semimajor axis $a(t)$ and semiminor axis $b(t)$. We denote the

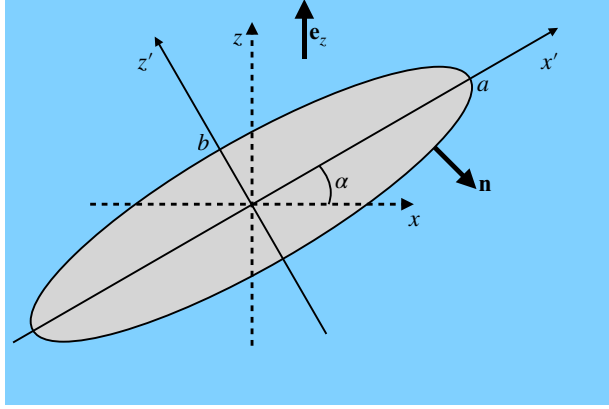


FIG. 14. Notation for dynamics of a tilted puller cluster. The deformed cluster is at every instant an ellipse of semimajor axis $a(t)$ and minor semiaxis $b(t)$. The flow is described in the x', z' coordinate system, rotated by an angle α relative to the laboratory coordinates x, z . The outwards unit normal to the cluster is denoted by \mathbf{n} and the vertical direction (along which stresslets are aligned) by \mathbf{e}_z .

angle with the x axis by $\alpha(t)$, and work in the rotated coordinate systems (x', z') [see Fig. 14 for a sketch with notation].

In order to match the viscous stress jump at the cluster's boundary, given explicitly by

$$\frac{S\phi_0}{V} \mathbf{e}_z (\mathbf{e}_z \cdot \mathbf{n}) = \frac{S\phi_0}{V} \sin^2(\alpha) \mathbf{n} + \frac{S\phi_0}{V} \cos(2\alpha) \mathbf{e}'_z (\mathbf{e}'_z \cdot \mathbf{n}) + \frac{S\phi_0}{2V} \sin(2\alpha) (\mathbf{e}'_x \mathbf{e}'_z + \mathbf{e}'_z \mathbf{e}'_x) \cdot \mathbf{n}, \quad (\text{E27})$$

we assume that the flow inside the cluster takes the form

$$\mathbf{u} = E(x' \mathbf{e}'_x - z' \mathbf{e}'_z) + \Omega_1 \left(\frac{x'}{a^2} \mathbf{e}'_z - \frac{z'}{b^2} \mathbf{e}'_x \right) + \Omega_2 (x' \mathbf{e}'_z - z' \mathbf{e}'_x), \quad (\text{E28})$$

with constant pressure p_0 . The first term (proportional to E) represents a straining flow aligned with the cluster. The second term (proportional to Ω_1) can be viewed as a rotational (“treadmilling”) flow, corresponding to a stretched solid-body rotation matching the elliptical cluster shape. Finally, the third term (proportional to Ω_2) corresponds to a rigid rotation of the whole cluster. Notice that, because the treadmilling term proportional to Ω_1 satisfies the no-penetration condition (as $\mathbf{n} \propto x' \mathbf{e}'_x / a^2 + z' \mathbf{e}'_z / b^2$), the flow \mathbf{u} does indeed exactly deform ellipses into ellipses.

By continuity of velocity, the external flow can be written as

$$\bar{\mathbf{u}} = -\mathbf{u}'_{\text{str}} - \mathbf{u}'_{\text{tr}} + \mathbf{u}_{\text{rot}}. \quad (\text{E29})$$

In Eq. (E29), \mathbf{u}'_{str} is the perturbation flow induced by a (fictitious) rigid ellipse $x'^2/a^2 + y'^2/b^2 = 1$ immersed in the background straining flow $\mathbf{u}_{\text{str}}^\infty = E(x' \mathbf{e}'_x - z' \mathbf{e}'_z)$, while \mathbf{u}'_{tr} is the perturbation flow induced by the same rigid ellipse immersed in the treadmilling flow $\mathbf{u}_{\text{tr}}^\infty = \Omega_1(x' \mathbf{e}'_z / a^2 - z' \mathbf{e}'_x / b^2)$. Finally, \mathbf{u}_{rot} is the flow induced by the same rigid ellipse when rotating in a fluid at rest. By construction, the flow in Eq. (E29) matches \mathbf{u} on the ellipse's boundary and decays as $\|\mathbf{x}'\| \rightarrow \infty$, so it must indeed be the external flow. Denoting by σ_{str} , σ_{tr} , σ_{rot} the stresses produced by the corresponding flows outside the fictitious ellipse, continuity of stress then takes the form

$$-p_0 \mathbf{n} + \sigma_{\text{str}} \cdot \mathbf{n} + \sigma_{\text{tr}} \cdot \mathbf{n} + \frac{S\phi_0}{V} \mathbf{e}_z (\mathbf{e}_z \cdot \mathbf{n}) = \sigma_{\text{rot}} \cdot \mathbf{n}. \quad (\text{E30})$$

Following the procedure laid out in Ref. [54], these stresses are found to be

$$\sigma_{\text{str}} \cdot \mathbf{n} = \frac{\mu E (a + b)^2}{ab} \mathbf{n} - \frac{2\mu E (a + b)^2}{ab} \mathbf{e}'_z (\mathbf{e}'_z \cdot \mathbf{n}), \quad (\text{E31a})$$

$$\boldsymbol{\sigma}_{\text{tr}} \cdot \mathbf{n} = \frac{2\mu\Omega_1}{ab}(\mathbf{e}'_z\mathbf{e}'_x - \mathbf{e}'_x\mathbf{e}'_z) \cdot \mathbf{n} - \frac{\mu(a^2 - b^2)\Omega_1}{a^2b^2}(\mathbf{e}'_x\mathbf{e}'_z + \mathbf{e}'_z\mathbf{e}'_x) \cdot \mathbf{n}, \quad (\text{E31b})$$

$$\boldsymbol{\sigma}_{\text{rot}} \cdot \mathbf{n} = \frac{2\mu b\Omega_2}{a}\mathbf{e}'_x(\mathbf{e}'_z \cdot \mathbf{n}) - \frac{2\mu a\Omega_2}{b}\mathbf{e}'_z(\mathbf{e}'_x \cdot \mathbf{n}). \quad (\text{E31c})$$

Stress-balance can thus be recast into

$$\begin{aligned} -p_0^- \mathbf{n} + \frac{\mu E(a+b)^2}{ab} \mathbf{n} - \frac{2\mu E(a+b)^2}{ab} \mathbf{e}'_z(\mathbf{e}'_z \cdot \mathbf{n}) + \frac{2\mu\Omega_1}{ab}(\mathbf{e}'_z\mathbf{e}'_x - \mathbf{e}'_x\mathbf{e}'_z) \cdot \mathbf{n} + \\ - \frac{\mu(a^2 - b^2)\Omega_1}{a^2b^2}(\mathbf{e}'_x\mathbf{e}'_z + \mathbf{e}'_z\mathbf{e}'_x) \cdot \mathbf{n} + \frac{S\phi_0}{V} \sin^2(\alpha) \mathbf{n} + \frac{S\phi_0}{V} \cos(2\alpha) \mathbf{e}'_z(\mathbf{e}'_z \cdot \mathbf{n}) \\ + \frac{S\phi_0}{2V} \sin(2\alpha)(\mathbf{e}'_x\mathbf{e}'_z + \mathbf{e}'_z\mathbf{e}'_x) \cdot \mathbf{n} = \frac{2\mu b\Omega_2}{a} \mathbf{e}'_x(\mathbf{e}'_z \cdot \mathbf{n}) - \frac{2\mu a\Omega_2}{b} \mathbf{e}'_z(\mathbf{e}'_x \cdot \mathbf{n}). \end{aligned} \quad (\text{E32})$$

Matching corresponding terms, we obtain the following simultaneous linear equations for p_0^- , E , Ω_1 , and Ω_2 , in terms of the stresslet strength S :

$$p_0^- - \frac{\mu E(a+b)^2}{ab} = \frac{S\phi_0}{V} \sin^2(\alpha), \quad (\text{E33a})$$

$$\frac{2\mu E(a+b)^2}{ab} = \frac{S\phi_0}{V} \cos(2\alpha), \quad (\text{E33b})$$

$$\frac{2\Omega_1\mu}{ab} - \frac{\mu(a^2 - b^2)\Omega_1}{a^2b^2} + \frac{2\mu a\Omega_2}{b} = -\frac{S\phi_0}{2V} \sin(2\alpha), \quad (\text{E33c})$$

$$\frac{2\Omega_1\mu}{ab} + \frac{\mu(a^2 - b^2)\Omega_1}{a^2b^2} + \frac{2\mu b\Omega_2}{a} = \frac{S\phi_0}{2V} \sin(2\alpha). \quad (\text{E33d})$$

Solving, we recover the expressions given in Eqs. (34) of the main text.

5. Numerical simulations of stretching puller clusters

a. Evolution of a 3D cluster

In this section, we present the details of the numerical scheme used to solve for the evolution of a 3D cluster in Sec. V of the main text. Because of the strong-alignment assumption ($\mathbf{p} \equiv \mathbf{e}_z$), the flow inside and outside the cluster obeys the Stokes equation, with the active stresses only appearing in the boundary condition $[\boldsymbol{\sigma}]_{\text{in}}^{\text{out}} \cdot \mathbf{n} = S\phi_0 \mathbf{e}_z(\mathbf{e}_z \cdot \mathbf{n})/V$. In order to simulate the stretching of a three-dimensional cluster of pullers (initially a sphere), we may therefore exploit the integral solution of the Stokes equations [45,46] to write

$$\dot{\mathbf{y}} = \frac{S\phi_0}{8\pi\mu V} \oint_{\partial V(t)} \left[\frac{\mathbf{e}_z}{r} + \frac{(\mathbf{x} - \mathbf{y})(\mathbf{x} - \mathbf{y})}{r^3} \cdot \mathbf{e}_z \right] (d\mathbf{S}_{\mathbf{x}} \cdot \mathbf{e}_z), \quad (\text{E34})$$

where \mathbf{y} is a point on the boundary ∂V , $d\mathbf{S}_{\mathbf{x}}$ is the inwards-pointing area vector, and $r := \|\mathbf{x} - \mathbf{y}\|$. In order to integrate Eq. (E34) numerically, we notice that the solution must be axisymmetric, and thus convert Eq. (E34) into a one-dimensional integral by performing the azimuthal integration analytically. To this end, we parametrize the axisymmetric surface at a given time point by $\{\mathbf{x} = R(z)\mathbf{e}_\rho + z\mathbf{e}_z : 0 \leq \theta \leq 2\pi, -L \leq z \leq L\}$ in cylindrical polars (ρ, θ, z) . We expect the range of z to be symmetrical about $z = 0$ by reflectional symmetry. In order to determine the evolution of the half-height L and the shape outline $R(z)$, we may limit our attention to the motion of points in the xz plane (by rotational symmetry). The velocity at any other point on the surface may thereafter be obtained by a suitable rotation. Suppose therefore that, in Eq. (E34), $\mathbf{y} = R_0\mathbf{e}_x + z_0\mathbf{e}_z$ with $R_0 \geq 0$, where $R_0 := R(z_0)$. We may evaluate the various geometrical quantities in Eq. (E34) as

$$d\mathbf{S}_{\mathbf{x}} = -R\mathbf{e}_\rho + RR'\mathbf{e}_z, \quad (\text{E35a})$$

$$r^2 = R^2 - 2R_0R \cos \theta + R_0^2 + (z - z_0)^2, \quad (\text{E35b})$$

$$(\mathbf{x} - \mathbf{y}) \cdot \mathbf{e}_z = z - z_0, \quad (\text{E35c})$$

$$(\mathbf{x} - \mathbf{y}) \cdot \mathbf{e}_x = R \cos \theta - R_0. \quad (\text{E35d})$$

By reflectional symmetry, the velocity at each point cannot have any azimuthal component. As for the remaining components, taking the components of Eq. (E34) along \mathbf{e}_x and \mathbf{e}_z we obtain

$$\mathbf{e}_x \cdot \dot{\mathbf{y}} = \frac{S\phi_0}{8\pi\mu V} \int_{-L}^L \left\{ \int_0^{2\pi} \frac{R \cos \theta - R_0}{r^3} d\theta \right\} (z - z_0) RR' dz, \quad (\text{E36a})$$

$$\mathbf{e}_z \cdot \dot{\mathbf{y}} = \frac{S\phi_0}{8\pi\mu V} \int_{-L}^L \left\{ \int_0^{2\pi} \left[\frac{1}{r} + \frac{(z - z_0)^2}{r^3} \right] d\theta \right\} RR' dz. \quad (\text{E36b})$$

The integrals in curly brackets are functions of z only, and may be evaluated in terms of elliptic integrals. To this end, we define

$$P(z) = [(R - R_0)^2 + (z - z_0)^2]^{1/2}, \quad (\text{E37a})$$

$$Q(z) = [(R + R_0)^2 + (z - z_0)^2]^{1/2}, \quad (\text{E37b})$$

and simplify Eqs. (E36a) and (E36b) by means of the identities

$$\int_0^{2\pi} \frac{d\theta}{r} = \frac{4}{P} \mathcal{K} \left(\frac{P^2 - Q^2}{P^2} \right), \quad (\text{E38a})$$

$$\int_0^{2\pi} \frac{d\theta}{r^3} = \frac{4}{PQ^2} \mathcal{E} \left(\frac{P^2 - Q^2}{P^2} \right), \quad (\text{E38b})$$

$$\int_0^{2\pi} \frac{\cos \theta}{r^3} d\theta = \frac{8}{P^3 - PQ^2} \mathcal{K} \left(\frac{P^2 - Q^2}{P^2} \right) - \left(\frac{4}{PQ^2} + \frac{8}{P^3 - PQ^2} \right) \mathcal{E} \left(\frac{P^2 - Q^2}{P^2} \right). \quad (\text{E38c})$$

In Eqs. (E38a) through (E38c), we defined

$$\mathcal{K}(m) = \int_0^{\pi/2} \frac{d\phi}{(1 - m \sin^2 \phi)^{1/2}}, \quad (\text{E39a})$$

$$\mathcal{E}(m) = \int_0^{\pi/2} (1 - m \sin^2 \phi)^{1/2} d\phi, \quad (\text{E39b})$$

with $m < 1$, to be the complete elliptic integrals of the first and second kind, respectively. Substituting into Eqs. (E36a) and (E36b), we finally obtain

$$\mathbf{e}_x \cdot \dot{\mathbf{y}} = \frac{S\phi_0}{8\pi\mu V} \int_{-L}^L (z - z_0) \mathcal{K}_1 RR' dz, \quad (\text{E40a})$$

$$\mathbf{e}_z \cdot \dot{\mathbf{y}} = \frac{S\phi_0}{8\pi\mu V} \int_{-L}^L \mathcal{K}_2 RR' dz, \quad (\text{E40b})$$

where the integration kernels \mathcal{K}_1 and \mathcal{K}_2 take the forms

$$\mathcal{K}_1 = \frac{8R}{P^3 - PQ^2} \mathcal{K} \left(\frac{P^2 - Q^2}{P^2} \right) - \left(\frac{4R}{PQ^2} + \frac{8R}{P^3 - PQ^2} \right) \mathcal{E} \left(\frac{P^2 - Q^2}{P^2} \right) - \frac{4R_0}{PQ^2} \mathcal{E} \left(\frac{P^2 - Q^2}{P^2} \right), \quad (\text{E41a})$$

$$\mathcal{K}_2 = \frac{4}{P} \mathcal{K} \left(\frac{P^2 - Q^2}{P^2} \right) + \frac{4(z - z_0)^2}{PQ^2} \mathcal{E} \left(\frac{P^2 - Q^2}{P^2} \right). \quad (\text{E41b})$$

The results in Eqs. (E40a) and (E40b) are now amenable to numerical integration. To this end, we focus on the slice of the boundary in the xz plane, with $x \geq 0$. Because the cluster is initially spherical, such a slice initially corresponds to a half-circle. We thereafter parametrize it via a cubic

spline and evolve the location of the nodes via the explicit second-order Adams-Bashforth method. We use the numerical cluster volume as a gauge for accuracy, ensuring that it never deviates by more than 1% from the initial value, as expected from incompressibility.

b. Evolution of a 2D cluster

In this section we present the details of the numerical scheme used to solve for the evolution of a 2D cluster in Sec. V of the main text. Similarly to the 3D case, we may express the velocity of points on the boundary as

$$\dot{\mathbf{y}} = \frac{S\phi_0}{\mu V} \oint_{\Gamma(t)} [\mathbf{J}(\mathbf{y} - \mathbf{x}) \cdot \mathbf{e}_z] (\mathbf{n} \cdot \mathbf{e}_z) ds, \quad (\text{E42})$$

where Γ is the corresponding horizontal slice of the cylinder, \mathbf{n} is the unit normal pointing into the cluster, and \mathbf{J} is the two-dimensional Green's function given by

$$\mathbf{J}(\mathbf{r}) = \frac{1}{4\pi} \left[-\mathbf{I} \log \|\mathbf{r}\| + \frac{\mathbf{r}\mathbf{r}}{\|\mathbf{r}\|^2} \right]. \quad (\text{E43})$$

We numerically integrate Eq. (E42) by discretizing the interface as a collection of N points, initially uniformly spaced around the unit circle, and stepping forward with the explicit second-order Adams-Bashforth method. The unit normal and arclength element at every point are evaluated with symmetric differences, while the integrable singularity in the kernel (E43) is regularized by approximating the Green's function with [55]

$$\begin{aligned} \mathbf{J}_\varepsilon(\mathbf{r}) = & \frac{1}{4\pi} \left[\ln(\sqrt{\|\mathbf{r}\|^2 + \varepsilon^2} + \varepsilon) - \frac{\varepsilon(\sqrt{\|\mathbf{r}\|^2 + \varepsilon^2} + 2\varepsilon)}{(\sqrt{\|\mathbf{r}\|^2 + \varepsilon^2} + \varepsilon)\sqrt{\|\mathbf{r}\|^2 + \varepsilon^2}} \right] \mathbf{I} \\ & + \frac{\sqrt{\|\mathbf{r}\|^2 + \varepsilon^2} + 2\varepsilon}{4\pi(\sqrt{\|\mathbf{r}\|^2 + \varepsilon^2} + \varepsilon)^2 \sqrt{\|\mathbf{r}\|^2 + \varepsilon^2}} \mathbf{r}\mathbf{r}. \end{aligned} \quad (\text{E44})$$

We took the regularization parameter to be $\varepsilon = 0.25 \times 2\pi/N$. We gauged the accuracy of the method by ensuring that the area of the deformed cluster never dropped below 95% of the initial area at each step, as expected from incompressibility.

APPENDIX F: SLENDER-BODY THEORY FOR 3D PUSHER JET

In this Appendix, we provide the derivation of Eqs. (41a) and (41b) in the main text. To this end, we must solve the jet equations (14a) through (16c), where \mathcal{P} is an elliptical cylinder with axis $\mathbf{x}(s) = \mathbf{x}(s_0) + s\mathbf{t}_1(s_0)$ ($-\infty < s < \infty$) and constant cross section $\mathcal{C}(s_0)$, given by

$$\mathcal{C}(s) = \{\mathbf{x}(s) + a(s) \cos(\eta)\mathbf{t}_1(s) + b(s) \sin(\eta)\mathbf{t}_2(s) : 0 \leq \eta < 2\pi\}. \quad (\text{F1})$$

Defining local Cartesian coordinates $\mathbf{x} - \mathbf{x}(s_0) = x_1\mathbf{t}_1 + x_2\mathbf{t}_2 + x_3\mathbf{t}_3$, the local flow inside the jet associated with this configuration is assumed to be a combination of axial shear and cross-sectional strain:

$$\mathbf{u} = \gamma x_1\mathbf{t}_3 + E(x_1\mathbf{t}_1 - x_2\mathbf{t}_2), \quad (\text{F2a})$$

$$\boldsymbol{\sigma} = -p_0\mathbf{I} + \gamma\mu(\mathbf{t}_1\mathbf{t}_3 + \mathbf{t}_3\mathbf{t}_1) + 2\mu E(\mathbf{t}_1\mathbf{t}_1 - \mathbf{t}_2\mathbf{t}_2), \quad (\text{F2b})$$

where p_0 is a constant. Letting \mathbf{n} be the local outwards unit normal to this cylinder, the flow is determined by continuity of velocity and the requirement that, on the boundary,

$$\boldsymbol{\sigma} \cdot \mathbf{n} + \frac{S\phi_0}{V} (\mathbf{e}_z \cdot \mathbf{n}) \mathbf{e}_z = \boldsymbol{\sigma}^{\text{ext}} \cdot \mathbf{n}. \quad (\text{F3})$$

1. Outer velocity field

The external flow, driven by the no-slip condition, is the negative of the perturbation flow created by a rigid elliptical cylinder in the unbounded flow $\mathbf{u}^\infty = \gamma x_1 \mathbf{t}_3 + E(x_1 \mathbf{t}_1 - x_2 \mathbf{t}_2)$. Equating the boundary stresses, we obtain that

$$\boldsymbol{\sigma}^\infty \cdot \mathbf{n} = -\frac{S\phi_0}{V}(\mathbf{e}_z \cdot \mathbf{n})\mathbf{e}_z \quad (\text{F4})$$

where $\boldsymbol{\sigma}^\infty \cdot \mathbf{n}$ is the traction on the rigid elliptical cylinder of cross section $\mathcal{C}(s_0)$ immersed in the flow \mathbf{u}^∞ . Expressing $\mathbf{e}_z = \mathbf{t}_3 \sin \zeta - \mathbf{t}_1 \cos \zeta$ in terms of the local material frame, and noting that $\mathbf{n} \cdot \mathbf{t}_3 = 0$, we can equivalently write

$$\boldsymbol{\sigma}^\infty \cdot \mathbf{n} = \frac{S\phi_0}{V}(\mathbf{t}_1 \cdot \mathbf{n})\left(\frac{1}{2}\mathbf{t}_3 \sin 2\zeta - \mathbf{t}_1 \cos^2 \zeta\right). \quad (\text{F5})$$

In Appendix F2, we show that

$$\boldsymbol{\sigma}^\infty \cdot \mathbf{n} = -p_1 \mathbf{n} + \frac{\mu E(1+\chi)^2}{\chi}(\mathbf{n} \cdot \mathbf{t}_1)\mathbf{t}_1 - \frac{\mu E(1+\chi)^2}{\chi}(\mathbf{n} \cdot \mathbf{t}_2)\mathbf{t}_2 + \frac{\mu \gamma(\chi+1)}{\chi}(\mathbf{n} \cdot \mathbf{t}_1)\mathbf{t}_3, \quad (\text{F6})$$

where p_1 is a constant. Assuming that Eq. (F6) is true, and writing $-p_1 \mathbf{n} = -p_1(\mathbf{n} \cdot \mathbf{t}_1)\mathbf{t}_1 - p_1(\mathbf{n} \cdot \mathbf{t}_2)\mathbf{t}_2$, Eq. (F5) yields the simultaneous equations

$$p_1 - \frac{\mu E(1+\chi)^2}{\chi} = \frac{S\phi_0 \cos^2 \zeta}{V}, \quad (\text{F7})$$

$$p_1 + \frac{\mu E(1+\chi)^2}{\chi} = 0, \quad (\text{F8})$$

$$\frac{\mu \gamma(1+\chi)}{\chi} = \frac{S\phi_0 \sin 2\zeta}{2V}, \quad (\text{F9})$$

which can be solved to yield Eqs. (41a) and (41b) in the main text.

2. Determining the stress

To conclude, we need to show that the stress on a rigid cylinder in the flow \mathbf{u}^∞ indeed takes the form (F6). The first term in Eq. (F6) corresponds to an isotropic pressure contribution, while the second and third term are obtained from (E11). The final term, as we will now show, is the traction on the elliptical cylinder exerted by an external shearing flow $\gamma x_1 \mathbf{t}_3$. To compute this traction, notice that the flow in the presence of the rigid cylinder must remain purely axial, with $\mathbf{u} = w(x_1, x_2)\mathbf{t}_3$. In the absence of any axial pressure gradients, we deduce that w satisfies

$$\nabla^2 w = 0 \quad \text{outside } \mathcal{C}, \quad (\text{F10a})$$

$$w = 0 \quad \mathbf{x} \in \mathcal{C}, \quad (\text{F10b})$$

$$w \sim \gamma x_1 \quad x_1^2 + x_2^2 \rightarrow \infty. \quad (\text{F10c})$$

Eqs. (F10a) through (F10c) may be solved in elliptic coordinates (τ, θ) , defined as

$$x_1 = c \cosh \tau \cos \theta, \quad (\text{F11a})$$

$$x_2 = c \sinh \tau \sin \theta, \quad (\text{F11b})$$

with $0 \leq \theta < 2\pi$, $0 \leq \tau < \infty$. The elliptical boundary \mathcal{C} corresponds to the level curve $\tau \equiv \tau_0$, where $\tanh(\tau_0) = \chi$ (the aspect ratio) and $c = a(1 - \chi^2)^{1/2}$. Furthermore, in elliptic coordinates, Laplace's equation takes the simple form

$$\frac{\partial^2 w}{\partial \tau^2} + \frac{\partial^2 w}{\partial \theta^2} = 0. \quad (\text{F12})$$

The solution to Eqs. (F10a) through (F10c) may now be determined from separation of variables, after noting that $w \sim \frac{1}{2}\gamma c e^\tau \cos \theta$ for $\tau \rightarrow \infty$. We find

$$w = \frac{1}{2}\gamma c(e^\tau - e^{2\tau_0-\tau}) \cos \theta, \quad (\text{F13})$$

with associated boundary stress

$$\begin{aligned} \boldsymbol{\sigma} \cdot \mathbf{e}_\tau|_{\tau=\tau_0} &= \frac{\mu}{c(\cosh^2 \tau_0 - \cos^2 \theta)^{1/2}} \frac{\partial w}{\partial \tau} \bigg|_{\tau=\tau_0} \mathbf{t}_3 \\ &= \frac{\mu \gamma e^{\tau_0} \cos \theta}{(\cosh^2 \tau_0 - \cos^2 \theta)^{1/2}} \mathbf{t}_3 \\ &= \frac{\mu \gamma e^{\tau_0}}{\sinh \tau_0} (\mathbf{n} \cdot \mathbf{t}_1) \mathbf{t}_3 \\ &= \frac{\mu \gamma (\chi + 1)}{\chi} (\mathbf{n} \cdot \mathbf{t}_1) \mathbf{t}_3. \end{aligned} \quad (\text{F14})$$

This is precisely the final term in Eq. (F6), completing our analysis.

-
- [1] D. L. Koch and G. Subramanian, Collective hydrodynamics of swimming microorganisms: Living fluids, *Annu. Rev. Fluid Mech.* **43**, 637 (2011).
 - [2] T. Ishikawa and T. J. Pedley, Coherent structures in monolayers of swimming particles, *Phys. Rev. Lett.* **100**, 088103 (2008).
 - [3] J. Elgeti, R. G. Winkler, and G. Gompper, Physics of microswimmers—Single particle motion and collective behavior: A review, *Rep. Prog. Phys.* **78**, 056601 (2015).
 - [4] T. Vicsek and A. Zafeiris, Collective motion, *Phys. Rep.* **517**, 71 (2012).
 - [5] P. Kraikivski, R. Lipowsky, and J. Kierfeld, Enhanced ordering of interacting filaments by molecular motors, *Phys. Rev. Lett.* **96**, 258103 (2006).
 - [6] I. Theurkauff, C. Cottin-Bizonne, J. Palacci, C. Ybert, and L. Bocquet, Dynamic clustering in active colloidal suspensions with chemical signaling, *Phys. Rev. Lett.* **108**, 268303 (2012).
 - [7] J. Wang, *Nanomachines: Fundamentals and Applications* (John Wiley & Sons, New York, 2013).
 - [8] D. Saintillan and M. J. Shelley, Instabilities and pattern formation in active particle suspensions: Kinetic theory and continuum simulations, *Phys. Rev. Lett.* **100**, 178103 (2008).
 - [9] D. Saintillan and M. J. Shelley, Instabilities, pattern formation, and mixing in active suspensions, *Phys. Fluids* **20**, 123304 (2008).
 - [10] D. Saintillan and M. J. Shelley, Active suspensions and their nonlinear models, *C. R. Phys.* **14**, 497 (2013).
 - [11] J. Dunkel, S. Heidenreich, K. Drescher, H. H. Wensink, M. Bär, and R. E. Goldstein, Fluid dynamics of bacterial turbulence, *Phys. Rev. Lett.* **110**, 228102 (2013).
 - [12] J. Stenhammar, C. Nardini, R. W. Nash, D. Marenduzzo, and A. Morozov, Role of correlations in the collective behavior of microswimmer suspensions, *Phys. Rev. Lett.* **119**, 028005 (2017).
 - [13] T. Arnoulx de Pirey, Y. Kafri, and S. Ramaswamy, Anomalous long-ranged influence of an inclusion in momentum-conserving active fluids, *Phys. Rev. X* **14**, 041034 (2024).
 - [14] C. R. Williams and M. A. Bees, Photo-gyrotactic bioconvection, *J. Fluid Mech.* **678**, 41 (2011).
 - [15] A. Théry, L. Le Nagard, J. Ono dit Biot, C. Fradin, K. Dálnoki-Veress, and E. Lauga, Self-organisation and convection of confined magnetotactic bacteria, *Sci. Rep.* **10**, 13578 (2020).
 - [16] W. M. Durham, J. O. Kessler, and R. Stocker, Disruption of vertical motility by shear triggers formation of thin phytoplankton layers, *Science* **323**, 1067 (2009).
 - [17] T. J. Pedley, N. A. Hill, and J. O. Kessler, The growth of bioconvection patterns in a uniform suspension of gyrotactic micro-organisms, *J. Fluid Mech.* **195**, 223 (1988).

- [18] T. J. Pedley and J. O. Kessler, A new continuum model for suspensions of gyrotactic micro-organisms, *J. Fluid Mech.* **212**, 155 (1990).
- [19] M. A. Bees, Advances in bioconvection, *Annu. Rev. Fluid Mech.* **52**, 449 (2020).
- [20] L. Fung, R. N. Bearon, and Y. Hwang, Bifurcation and stability of downflowing gyrotactic micro-organism suspensions in a vertical pipe, *J. Fluid Mech.* **902**, A26 (2020).
- [21] J. O. Kessler, Hydrodynamic focusing of motile algal cells, *Nature (Lond.)* **313**, 218 (1985).
- [22] P. Denissenko and S. Lukaschuk, Velocity profiles and discontinuities propagation in a pipe flow of suspension of motile microorganisms, *Phys. Lett. A* **362**, 298 (2007).
- [23] L. Fung, Analogy between streamers in sinking spheroids, gyrotactic plumes and chemotactic collapse, *J. Fluid Mech.* **961**, A12 (2023).
- [24] J. S. Font-Muñoz, R. Jeanneret, J. Arrieta, S. Anglès, A. Jordi, I. Tuval, and G. Basterretxea, Collective sinking promotes selective cell pairing in planktonic pennate diatoms, *Proc. Natl. Acad. Sci. USA* **116**, 15997 (2019).
- [25] D. L. Koch and E. S. G. Shaqfeh, The instability of a dispersion of sedimenting spheroids, *J. Fluid Mech.* **209**, 521 (1989).
- [26] X. Garcia, S. Rafai, and P. Peyla, Light control of the flow of phototactic microswimmer suspensions, *Phys. Rev. Lett.* **110**, 138106 (2013).
- [27] L. Jibuti, L. Qi, C. Misbah, W. Zimmermann, S. Rafai, and P. Peyla, Self-focusing and jet instability of a microswimmer suspension, *Phys. Rev. E* **90**, 063019 (2014).
- [28] A. M. Metcalfe and T. J. Pedley, Falling plumes in bacterial bioconvection, *J. Fluid Mech.* **445**, 121 (2001).
- [29] J. O. Kessler, Gyrotactic buoyant convection and spontaneous pattern formation in algal cell cultures, in *Nonequilibrium Cooperative Phenomena in Physics and Related Fields* (Springer, Berlin, 1984), pp. 241–248.
- [30] T. Ishikawa, T. N. Dang, and E. Lauga, Instability of an active fluid jet, *Phys. Rev. Fluids* **7**, 093102 (2022).
- [31] O. S. Pak and E. Lauga, Generalized squirming motion of a sphere, *J. Eng. Math.* **88**, 1 (2014).
- [32] K. Drescher, J. Dunkel, L. H. Cisneros, S. Ganguly, and R. E. Goldstein, Fluid dynamics and noise in bacterial cell–cell and cell–surface scattering, *Proc. Natl. Acad. Sci. USA* **108**, 10940 (2011).
- [33] K. Drescher, R. E. Goldstein, N. Michel, M. Polin, and I. Tuval, Direct measurement of the flow field around swimming microorganisms, *Phys. Rev. Lett.* **105**, 168101 (2010).
- [34] J. Rayleigh, On the stability, or instability, of certain fluid motions, *Proc. Lond. Math. Soc.* **11**, 57 (1880).
- [35] E. Lauga, T. N. Dang, and T. Ishikawa, Zigzag instability of biased pusher swimmers, *EPL* **133**, 44002 (2021).
- [36] E. Lauga and F. Nadal, Clustering instability of focused swimmers, *Europhys. Lett.* **116**, 64004 (2017).
- [37] I. Eisenmann, M. Vona, N. Desprat, T. Ishikawa, E. Lauga, and R. Jeanneret, companion paper, Pure hydrodynamic instabilities in active jets of puller microalgae, *Phys. Rev. Lett.* **135**, 198301 (2025).
- [38] L. Fung, R. N. Bearon, and Y. Hwang, A local approximation model for macroscale transport of biased active brownian particles in a flowing suspension, *J. Fluid Mech.* **935**, A24 (2022).
- [39] G. K. Batchelor, The stress system in a suspension of force-free particles, *J. Fluid Mech.* **41**, 545 (1970).
- [40] D. Saintillan, Rheology of active fluids, *Annu. Rev. Fluid Mech.* **50**, 563 (2018).
- [41] G. B. Arfken and H. J. Weber, *Mathematical Methods for Physicists*, 6th ed. (Elsevier Academic Press, London, 2005).
- [42] G. N. Watson, *A Treatise on the Theory of Bessel Functions* (Cambridge University Press, Cambridge, 1922).
- [43] G. S. Klindt and B. M. Friedrich, Flagellar swimmers oscillate between pusher-and puller-type swimming, *Phys. Rev. E* **92**, 063019 (2015).
- [44] Y. Shoham and N. Oppenheimer, Hamiltonian dynamics and structural states of two-dimensional active particles, *Phys. Rev. Lett.* **131**, 178301 (2023).
- [45] J. Happel and H. Brenner, *Low Reynolds Number Hydrodynamics: With Special Applications to Particulate Media*, Vol. 1 (Springer Science & Business Media, New York, 1983).

- [46] S. Kim and S. J. Karrila, *Microhydrodynamics: Principles and Selected Applications* (Butterworth-Heinemann, Oxford, 2013).
- [47] E. Lauga and S. Michelin, Stresslets induced by active swimmers, *Phys. Rev. Lett.* **117**, 148001 (2016).
- [48] T. Ishikawa, Vertical dispersion of model microorganisms in horizontal shear flow, *J. Fluid Mech.* **705**, 98 (2012).
- [49] I. Eisenmann, A. L’Homme, A. Lahlou, S. Bujaldon, T. L. Saux, B. Bailleul, N. Desprat, and R. Jeanneret, Light-induced phase separation with finite wavelength selection in photophobic microalgae, *Phys. Rev. Lett.* **135**, 148401 (2025).
- [50] See Supplemental Material at <http://link.aps.org/supplemental/10.1103/pbzf-svnr> for Movies S1 and S2.
- [51] K. C. Leptos, M. Chioccioli, S. Furlan, A. I. Pesci, and R. E. Goldstein, Phototaxis of *chlamydomonas* arises from a tuned adaptive photoresponse shared with multicellular volvocine green algae, *Phys. Rev. E* **107**, 014404 (2023).
- [52] C. J. Miles, A. A. Evans, M. J. Shelley, and S. E. Spagnolie, Active matter invasion of a viscous fluid: Unstable sheets and a no-flow theorem, *Phys. Rev. Lett.* **122**, 098002 (2019).
- [53] M. Vona, I. Eisenmann, N. Desprat, R. Jeanneret, T. Ishikawa, and E. Lauga, Supporting data for “Hydrodynamic instabilities of active jets,” [10.6084/m9.figshare.30122074](https://doi.org/10.6084/m9.figshare.30122074) (2025).
- [54] K. F. Mulchrone and K. Walsh, The motion of a non-rigid ellipse in a general 2d deformation, *J. Struct. Geol.* **28**, 392 (2006).
- [55] R. Cortez, The method of regularized stokeslets, *SIAM J. Sci. Comput.* **23**, 1204 (2001).